J. Fluid Mech. (2005), *vol.* 542, *pp.* 305–342.
doi:10.1017/S0022112005006427 Printed in the United Kingdom

The effect of rotation on rapidly sheared homogeneous turbulence and passive scalar transport. Linear theory and direct numerical simulation

By G. BRETHOUWER

Department of Mechanics, KTH, SE-100 44 Stockholm, Sweden
geert@mech.kth.se

(Received 7 November 2003 and in revised form 2 June 2005)

The effect of rotation on a homogeneous turbulent shear flow has been studied by means of a series of direct numerical simulations with different rotation numbers. The evolution of passive scalar fields with mean gradients in each of the three orthogonal directions in the flow was investigated in order to elucidate the effect of rotation on turbulent scalar transport. Conditions of the near-wall region of a boundary layer were approached by using a rapid shear and therefore, comparisons could be made with rapid distortion theory based on the linearized equations of the flow and scalar transport. Reynolds stresses, pressure–strain correlations and two-point velocity correlations were computed and turbulent structures were visualized. It is shown that rotation has a strong influence on the time development of the turbulent kinetic energy, the anisotropy of the flow and on the turbulent structures. Furthermore, rotation significantly affects turbulent scalar transport. The transport rate of the scalar and the direction of the scalar flux vector show large variations with different rotation numbers, and a strong alignment was observed between the scalar flux and the principal axes of the Reynolds stress tensor. The ratio of the turbulent and scalar time scales is influenced by rotation as well. The predictions of the linear theory of the turbulent one-point statistics and the scalar flux agreed fairly well with direct numerical simulation (DNS) results based on the full nonlinear governing equations. Nonetheless, some clear and strong nonlinear effects are observed in a couple of cases which significantly influence the development of the turbulence and scalar transport.

1. Introduction

Flows of gases and liquids often take place in a rotating system. The so-called Coriolis force in this rotating system acts on the fluid and this gives rise to complicated but interesting phenomena. Flow patterns can alter owing to the influence of rotation, and also the turbulent characteristics change if there is rotation, which has been proved by several experimental and numerical studies (see Bech & Anderson 1997 and references therein). It is more than likely that the alteration of the turbulence by rotation, in its turn, will affect the transport and dispersion of scalars, for example pollutants, heat and reacting species. For practical situations, it is of considerable importance to know how rotation affects turbulent flows and how rotation affects transport and dispersion of scalars in turbulent flows.

In recent years, the modelling of rotating turbulent flows or flows with streamline curvature received considerable attention, see for instance the studies of Speziale, Younis & Berger (2000), Poroseva *et al.* (2002), Wallin & Johansson (2002) and Gatski & Wallin (2004), but an accurate description of rotational effects remains a difficult subject.

Salhi & Cambon (1997) and Salhi (2002) studied the most basic case with both shear and rotation, namely homogeneous turbulent shear flow in a rotating frame. They used linear rapid distortion theory (RDT) to investigate the influence of the rotation on the development of the flow. Assuming a linear shear flow with shear rate S, and a rotation around the spanwise axis, with angular velocity Ω, Salhi & Cambon showed that maximum destabilization of the flow occurs at $R = 2\Omega/S = -1/2$. (For convenience we take $U_i = S\,x_3\,\delta_{i1}$ as we do later in the paper.) Moreover, they analysed the influence of pressure on the turbulence development and compared the results of RDT with large-eddy simulation (LES) of rotating homogeneous shear flow performed by Bardina, Ferziger & Reynolds (1983) and found a reasonable agreement. In contrast to a pressureless analysis, RDT reveals a difference between the cases R and $-1-R$ regarding the growth of the kinetic energy. Salhi (2002) presents analytical solutions for the RDT equations and some statistical quantities.

Lee, Kim & Moin (1990) studied homogeneous turbulent shear flow with a high shear rate, but without rotation, through direct numerical simulations (DNS). The value of the non-dimensional shear number SK/ε, where K is the turbulent kinetic energy and ε is the energy dissipation, was approximately 17 in their simulations. This is of the same order as the value of the non-dimensional shear number in the buffer region of a turbulent boundary layer. Lee *et al.* observed in the rapidly sheared homogeneous flow, streaky turbulent structures, similar to the structures found in turbulent boundary layers, and concluded that a high shear rate is the most important requirement for the generation of turbulent streaks and not the presence of a wall. In their study the RDT predictions of the anisotropy of the Reynolds stresses agreed well with the DNS data at these high shear rates. RDT was also able to describe the development of the turbulent structures, showing the importance of linear effects for the dynamics of rapidly sheared homogeneous turbulent flows.

Passive scalar transport in non-rotating shear flows has received considerable attention during the last few decades. Tavoularis & Corrsin (1981) and Rogers, Mansour & Reynolds (1989) investigated passive scalar mixing with a uniform mean scalar gradient in homogeneous turbulent shear flow. In the case of a scalar field with a mean gradient in the transverse direction, they observed a much larger scalar flux in the flow direction than in the transverse direction, leading to a strong misalignment between the scalar flux vector and the mean scalar gradient. Consequently, gradient-diffusion models are not the most appropriate models to describe the turbulent scalar flux in homogeneous shear flow because they assume alignment between the scalar flux and the mean gradient. An alternative modelling approach, algebraic scalar flux modelling, has in the case of homogeneous and other turbulent shear flows considerably more success in predicting the correct scalar flux (Rogers *et al.* 1989; Abe, Kondoh & Nagano 1996; Wikström, Wallin & Johansson 2000; Högström, Wallin & Johansson 2001).

Detailed studies of scalar transport in rotating shear flows are, nevertheless, rare. Nagano & Hattori (2003) and Wu & Kasagi (2004) studied, through DNS, scalar transport in a rotating turbulent channel flow at a low Reynolds number. The correlation between the wall-normal velocity fluctuations and scalar fluctuations

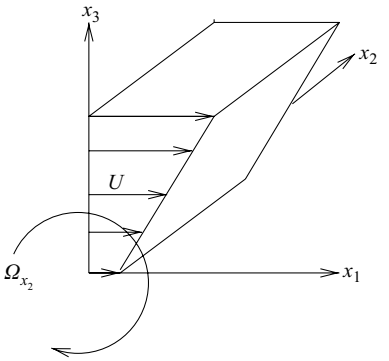

FIGURE 1. Sketch of the mean velocity profile, coordinate system and the direction of rotation.

changes with varying rotation numbers according to this study. Further detailed investigations of the influence of rotation on turbulent scalar transport are lacking.

In this paper, a study is presented of homogeneous turbulent shear flow with a passive scalar field in a rotating frame at different rotation numbers. Direct numerical simulations (DNS) and linear theory are used in this investigation. A linear and steady mean scalar gradient is imposed and high shear rates are used with the aim of approximating the conditions in a turbulent boundary close to the wall. The main objective of the study is to clarify the following points. How are the development of turbulence and, in particular, the anisotropy and the turbulent structures affected by rotation? What is the influence of rotation on turbulent scalar transport? To find an answer to these questions results on scalar fluctuations, scalar–velocity correlations and scalar dissipation will be presented. Furthermore, how important are linear processes for the development of turbulence and for scalar mixing in a rapidly sheared turbulent flow and can a linear model explain the influence of rotation on turbulence and scalar mixing? To investigate these aspects, detailed comparisons between linear theory and the DNS data will be made.

2. Geometry and governing equations

The governing equations of the incompressible homogeneous turbulent shear flow in a rotating frame are

$$\nabla \cdot \boldsymbol{u} = 0, \tag{2.1}$$

$$\frac{\partial \boldsymbol{u}}{\partial t} + \boldsymbol{u} \cdot \nabla \boldsymbol{u} + Sx_3 \frac{\partial \boldsymbol{u}}{\partial x_1} + Su_3 \boldsymbol{e}_1 + 2\boldsymbol{\Omega} \times \boldsymbol{u} = -\nabla p + \nu \nabla^2 \boldsymbol{u}, \tag{2.2}$$

where $\boldsymbol{u}$ is the fluctuating velocity, ∇p is the sum of the pressure gradient and the centrifugal force, both divided by the fluid density, ν is the viscosity, $S = \partial \overline{U}_1 / \partial x_3$ is the imposed linear mean velocity gradient, $\boldsymbol{\Omega}$ is the rotation vector and $\boldsymbol{e}_i$ is the unit vector in the x_i-direction. The last term on the left-hand side of the equation represents the Coriolis force. In the present case, the frame is rotating around the spanwise axis and thus $\boldsymbol{\Omega} = \Omega \boldsymbol{e}_2$ with Ω being the angular velocity of the frame. The mean velocity profile, coordinate system and direction of rotation are sketched in figure 1.

Using these equations, we can derive the Reynolds stress evolution equations,

$$\frac{\partial \overline{u_1 u}_1}{\partial t} = -2\,\overline{u_1 u}_3\, S\,(1+R) + \Pi_{11} - \varepsilon_{11}, \tag{2.3}$$

$$\frac{\partial \overline{u_2 u}_2}{\partial t} = \Pi_{22} - \varepsilon_{22}, \tag{2.4}$$

$$\frac{\partial \overline{u_3 u}_3}{\partial t} = 2\,\overline{u_1 u}_3\, S\, R + \Pi_{33} - \varepsilon_{33}, \tag{2.5}$$

$$\frac{\partial \overline{u_1 u}_3}{\partial t} = \overline{u_1 u}_1\, S\, R - \overline{u_3 u}_3\, S\,(1+R) + \Pi_{13} - \varepsilon_{13}, \tag{2.6}$$

where Π_{ij} and ε_{ij} denote the usual pressure–strain correlation and dissipation rates, respectively, and $R = 2\Omega/S$. The pressure–strain correlation redistributes the energy between the different fluctuating velocity components and can be split into a slow part, related to nonlinear processes, and a rapid part, related to the large-scale distortion of the flow. The Poisson equation for the rapid and slow part of the pressure, respectively, satisfy in our case

$$\nabla^2 p^{(r)} = (-2S - 2\Omega)\frac{\partial u_3}{\partial x_1} + 2\Omega\frac{\partial u_1}{\partial x_3}, \tag{2.7}$$

$$\nabla^2 p^{(s)} = -\frac{\partial u_i}{\partial x_j}\frac{\partial u_j}{\partial x_i}. \tag{2.8}$$

In Appendix A, the stability of rotating homogeneous shear flow is analysed using the Reynolds stress equations without the pressure–strain correlations and dissipation terms. This is a drastic simplification, but nevertheless, the analysis gives a reasonable qualitative picture of the stability as a function of the rotation number. The conclusions of the analysis are that (i) the turbulent kinetic energy grows algebraically if $R = 0$ or $R = -1$, (ii) the flow is destabilized by rotation if $-1 < R < 0$ with an exponentially growing kinetic energy and with at maximum destabilization at $R = -1/2$, (iii) the Reynolds stresses have an oscillating behaviour and the turbulence is stabilized by rotation if $R < -1$ or $R > 0$.

Using (2.2) we can derive for the fluctuating vorticity $\boldsymbol{\omega}$ the following equation,

$$\frac{\partial \omega_i}{\partial t} + u_k\frac{\partial \omega_i}{\partial x_k} + Sx_3\frac{\partial \omega_i}{\partial x_1} = \omega_k\frac{\partial u_i}{\partial x_k} + \nu\nabla^2\omega_i + S\omega_3\delta_{i1} + S(1+R)\frac{\partial u_i}{\partial x_2}. \tag{2.9}$$

The second and third terms on the left-hand side of the equation are the advection by the fluctuating and mean velocity. The first term on the right-hand side is the nonlinear production of vorticity, the third and last terms are the linear production of vorticity.

In the homogeneous turbulent shear flow we study the turbulent transport of a passive scalar with an imposed mean and linear scalar gradient $\boldsymbol{G}$. The transport equation for the fluctuation of the passive scalar θ, which does not have an influence on the velocity field, is given by

$$\frac{\partial \theta}{\partial t} + \boldsymbol{u}\cdot\nabla\theta + Sx_3\frac{\partial \theta}{\partial x_1} + \boldsymbol{G}\cdot\boldsymbol{u} = \kappa\nabla^2\theta, \tag{2.10}$$

where κ is the molecular diffusivity of the scalar. The last term on the left-hand side is a production term of scalar fluctuations. The effect of rotation does not directly enter the scalar equation, but scalar transport is, nevertheless, affected by rotation because of the alteration of the velocity field by rotation. This can be noticed when

the transport equation for the mean turbulent scalar flux is considered, which for the present rotating homogeneous shear flow reads

$$\frac{\partial \overline{u_i\theta}}{\partial t} = -\overline{u_i u_j}\, G_j - \overline{u_3\theta}\, S\, \delta_{i1} + 2\,\epsilon_{ij2}\, \overline{u_j\theta}\, \Omega + \Pi_{\theta i} - \varepsilon_{\theta i}. \tag{2.11}$$

Here, the first and second terms on the right-hand side are production terms due to mean gradients, $\Pi_{\theta i}$ the pressure-scalar–gradient correlation and $\varepsilon_{\theta i}$ the viscous and diffusive destruction term, see e.g. Wikström *et al.* 2000. The third term is a direct consequence of the rotation and affects, in the present case, the scalar flux in the streamwise and transverse directions. This is, however, not the only term influenced by rotation. Reynolds stresses and the pressure field are also affected by rotation, as we will see later, and therefore the first and fourth terms on the right-hand side can change as well.

3. Direct numerical simulations

The governing equations of the three-dimensional turbulent flow and scalar transport given by (2.2) and (2.10), respectively, are solved with a pseudospectral method with periodic boundary conditions on the computational domain. The aliasing errors are reduced by a combination of phase shifting and truncation. Only after $St = 10$ at $R = 0$, series B, were the aliasing errors completely removed by employing the 2/3 rule. A fourth-order or a low-storage third-order Runge–Kutta scheme is used for the time advancement of the nonlinear terms, and the linear viscous and diffusive terms are integrated exactly in Fourier wavenumber space. In order to be able use periodic boundary conditions in all three directions, a coordinate transformation was employed and consequently the numerical grid moved with the mean flow field. To avoid large deformations of the grid, it is remeshed with regular time intervals at times $(m + 1/2)\,(L_{x_1}/L_{x_3})\,S^{-1} (m = 0, 1, 2, \ldots)$ where L_{x_i} is the size of the domain in the x_i-direction. The same procedure has been used by Rogers *et al.* (1989). During the remeshing, some information is lost, especially at high wavenumbers, but this was in general quite small in the present simulations. The loss of kinetic energy was in fact negligible. The loss of energy dissipation was more serious, but, for example, in the run without system rotation series B the decrease of energy dissipation during remeshing was not larger than 1.5 %. Statistics were computed when the coordinate system was non-skewed.

The numerical code has been thoroughly validated by comparing it with an independently written code. The two codes produced essentially the same results for the velocity and scalar field and the small differences could be attributed to the different time-integration methods used. Also, case $C128U$ of Rogers, Moin & Reynolds (1986) has been repeated and the major results concerning velocity and scalar statistics could be reproduced.

The initial approximately isotropic velocity field for the present simulations has been obtained from a DNS of decaying isotropic turbulence and has a Taylor Reynolds number of $Re_\lambda = u'\lambda/\nu = 32$ where u' is the root mean square (r.m.s.) of the velocity fluctuations and λ is the Taylor length scale.

Five cases with different rotation numbers have been simulated: $R = 2\Omega/S = 0$ (pure shear), $R = -1/2$, $R = -1$ (zero absolute mean vorticity), $R = -3/2$ and $R = 1/2$. The numerical parameters used in the simulations are given in table 1. Each case has been simulated twice (series A and series B), with different numbers of grid points and

$R = 2\Omega/S$ *Series A*	L_{x_2}	S	$N_1 \times N_2 \times N_3$	ℓ	L	$k_{max}\eta$
0	3.11π	51.8	$576 \times 448 \times 288$	0.288	0.284	1.60
$-1/2$	3.11π	51.8	$576 \times 448 \times 288$	0.288	0.284	1.60
-1	2.5π	47.46	$512 \times 320 \times 256$	0.295	0.296	1.49
$-3/2$	2.5π	47.46	$512 \times 320 \times 256$	0.295	0.296	1.49
$1/2$	3π	46.6	$512 \times 384 \times 256$	0.298	0.299	1.50
Series B						
0	3π	75.5	$768 \times 640 \times 512$	0.194	0.235	1.47
$-1/2$	3π	75.5	$768 \times 640 \times 512$	0.194	0.235	1.47
-1	3π	75.5	$640 \times 480 \times 384$	0.194	0.235	1.47
$-3/2$	3π	94.2	$576 \times 440 \times 352$	0.172	0.214	1.17
$1/2$	3π	94.2	$576 \times 440 \times 352$	0.172	0.214	1.17

TABLE 1. Overview of the numerical parameters that have been used. Only the size of the domain in the spanwise direction and L_{x_2} has been varied. The size of the computational domain in the streamwise and transverse direction, equal to 4π and 2π, respectively, has been kept constant in all simulations. N_i is the number of nodes in the x_i-direction, ℓ is the longitudinal integral length scale and $L = u'^3/\varepsilon$ of the initial isotropic velocity field, $k_{max}\eta$ is the largest resolved wavenumber multiplied by the Kolmogorov length scale at $t = 0$.

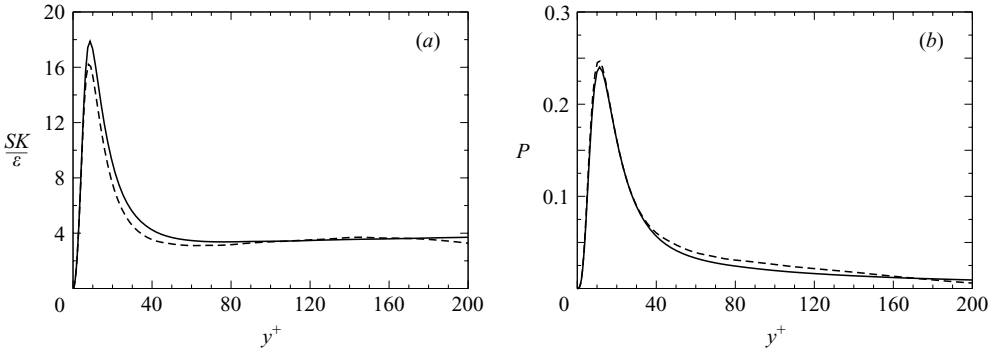

FIGURE 2. (*a*) SK/ε and (*b*) production of turbulent kinetic energy normalized with wall units as a function of the non-dimensional distance to the wall y^+ in terms of wall units.Solid line:, channel flow data (Moser *et al.* 1999); dashed line:, boundary-layer data (Komminaho & Skote 2002).

domain sizes, in order to investigate whether the results are significantly affected by the finite size of the domain, remeshing and resolution.

The conditions in a turbulent boundary layer close to the wall were approximated by choosing an appropriate shear rate. Figure 2(*a*) presents the non-dimensional shear number SK/ε obtained from DNS data of turbulent channel flow at $Re_\tau = 590$ (Moser, Kim & Mansour 1999) and a zero-pressure-gradient turbulent boundary layer (Komminaho & Skote 2002) as a function of the distance to the wall. According to these simulations, SK/ε has a high value in the buffer layer with a maximum value between 16 and 18 at about $y^+ = 10$. This is also approximately the position where the production rate of turbulent kinetic energy has its highest value, as shown in figure 2(*b*). In order to approximate the conditions in the important part of the boundary layer where most of the kinetic energy is produced, we have set the initial value of non-dimensional shear number SK/ε in all simulations to 18. Note that

this value is much larger than the asymptotic non-dimensional shear number in a homogeneous turbulent shear flow which is believed to be close to 6 (Tavoularis & Karnik 1989) and the equilibrium state will therefore not be reached in the present numerical simulations. Hence, it is natural that the non-dimensional shear number does not stay constant during the simulations, but varies. At $R=0$, $R=-1/2$ and $R=-1$, the minimum value reached by SK/ε up to the non-dimensional time $St=8$, was 13. After $St=8$, SK/ε decreased slightly to 11.8 at $R=0$. At $R=-3/2$ and $R=1/2$, SK/ε reached lower values but stayed above 8.9.

In series *A*, transport equations for three passive scalars are solved, together with the flow equations. The three scalars all have a Schmidt number of $\nu/\kappa=0.7$ and have a mean scalar gradient in the x_1-, x_2- and x_3-directions, respectively. The evolution for any mean scalar gradient is a simple superposition of these three passive scalar fields. In series *B*, only the evolution of one scalar field with a mean gradient in the x_3-direction has been simulated. The initial scalar fields are without scalar fluctuations, but the mean gradient acts as a source of fluctuations.

During the simulations, the turbulent length scales grow and eventually become too large for the finite domain we use in the DNS. In order to be sure that the DNS results do not depend on the size of the physical domain, we have carefully followed the development of the two-point velocity correlations during the computations and stopped the simulations as soon as the correlations did not properly approach zero for increasing separation distances.

While the largest scales tend to grow, the Kolmogorov length scale η becomes, in general, smaller during the simulations which makes higher demands on the grid spacing. In series *A*, $k_{max}\eta$, where k_{max} is the largest resolved wavenumber, was always equal to or larger than 1.0 during the simulations, except in the $R=-1/2$ case, series *A*, where $k_{max}\eta=0.93$ at the end of the simulations at $St=6$. To save computation time, a coarser grid was used in series *B* at $R=0$ and $R=-1/2$ initially, but, in the last part of the simulations, the resolution was increased to the values reported in table 1. During the simulations $k_{max}\eta$ was, however, always smaller than one.

4. Linearized equations

If the shear or rotation rate is high enough, the Navier–Stokes equations and the transport equation of the scalar can be approximated by their linearized forms. The assumption of linearity is the main idea behind rapid distortion theory (RDT).

The necessary requirement for the applicability of RDT on the flow field in the present case is that in (2.2) the nonlinear term is much smaller than either the linear term due to mean shear or the term due to rotation. Using a characteristic eddy size l and eddy velocity u, the order of the nonlinear term can be estimated as

$$|\boldsymbol{u}\cdot\nabla\boldsymbol{u}| = O(u^2/l),$$

and the linear mean shear and rotation term can be estimated as

$$|Su_3\boldsymbol{e}_1| = O(Su), \qquad |2\boldsymbol{\Omega}\times\boldsymbol{u}| = O(\Omega u),$$

respectively. The energy-containing scales can be approximated by $u\simeq K^{1/2}$ and $l\simeq K^{3/2}/\varepsilon$ and hence, the necessary condition for the applicability of RDT becomes either $SK/\varepsilon\gg 1$ or $\Omega K/\varepsilon\gg 1$. In other words, the time scale of the turbulence must be much larger than the time scale of shear or rotation and this condition is satisfied in all present simulations, at least for the large scales. We can thus expect a reasonable prediction of RDT of the large-scale turbulence characteristics such as anisotropy.

For the smaller turbulent scales, the time scale is shorter and the applicability of RDT is questionable. Furthermore, we must stress that the condition $SK/\varepsilon \gg 1$ or $\Omega K/\varepsilon \gg 1$ is a necessary condition, but not always a sufficient condition, as we will see later in this paper.

For the scalar, the necessary condition for the applicability of RDT is that the second advection term in (2.10) is much smaller than the fourth term owing to the mean scalar gradient. These terms can be estimated as

$$|\boldsymbol{u}\cdot\nabla\theta| = O(u\theta'/l)$$

and

$$|\boldsymbol{G}\cdot\boldsymbol{u}| = O(Gu),$$

respectively, where θ' is the root mean square of the scalar fluctuations. The condition for RDT becomes then $(GK^{3/2})/(\theta'\varepsilon) \gg 1$. In § 5, we will observe that $(\theta'/G)/(u/S)$ is $O(1)$ or larger after short distortion times. Assuming that the ratio is $O(1)$, the condition for the scalar becomes $SK/\varepsilon \gg 1$, which is in fact the same as for the flow field. In the case where $(\theta'/G)/(u/S)$ is not $O(1)$ but larger, the condition $SK/\varepsilon \gg 1$ is not necessarily sufficient and the more severe demand $(GK^{3/2})/(\theta'\varepsilon) \gg 1$ applies. The condition for the applicability of RDT for scalar transport therefore seems more restrictive than for the flow field.

In cases of homogeneous flow, the governing equations for the flow and scalar field can be transformed to Fourier space with the definitions

$$u_i = \sum_{\boldsymbol{k}} \hat{u}_i(\boldsymbol{k}, t)\mathrm{e}^{\mathrm{i}\boldsymbol{k}\cdot\boldsymbol{x}} \quad (i = 1, 2, 3) \tag{4.1}$$

and

$$\theta = \sum_{\boldsymbol{k}} \hat{\theta}(\boldsymbol{k}, t)\mathrm{e}^{\mathrm{i}\boldsymbol{k}\cdot\boldsymbol{x}} \tag{4.2}$$

After the linearization, elimination of the pressure using the continuity equation and transformation to a coordinate system moving with the mean flow, the RDT equations for the homogeneous shear flow read

$$\left(\frac{\mathrm{d}}{\mathrm{d}St} + \nu\frac{k^2}{S}\right)\hat{u}_i = -\underbrace{\left[\left(\delta_{i1} - 2\frac{k_i k_1}{k^2}\right)\delta_{j3} - 2\frac{\Omega}{S}\left(\epsilon_{ij2} - \frac{k_i k_n}{k^2}\epsilon_{nj2}\right)\right]}_{\mathscr{D}_{ij}}\hat{u}_j, \tag{4.3}$$

and for the scalar fluctuation with a mean gradient

$$\left(\frac{\mathrm{d}}{\mathrm{d}St} + \kappa\frac{k^2}{S}\right)\hat{\theta} = -\frac{G_i}{S}\hat{u}_i, \tag{4.4}$$

where the time t is scaled with the shear rate and ϵ_{ijk} is the permutation tensor. The wavenumbers evolve according to

$$\frac{\mathrm{d}k_i}{\mathrm{d}St} = -k_1\delta_{i3}. \tag{4.5}$$

The viscous and diffusive terms are not neglected in the present analysis, but have been taken into account in the RDT computations.

To compute the Reynolds stresses, scalar fluxes and other mean statistical moments, the Fourier coefficients of the velocity and scalar have to be integrated in wavenumber space. However, in the present study, the viscous and diffusive terms are retained and

therefore, an initial turbulent energy spectrum must be specified. For the scalar field, no initial spectrum need be specified because the fluctuations are initially zero, similar to the initial conditions of the DNS. The following form is assumed for the initial energy spectrum

$$E(k') = Ck'^2 \exp(-2k'l) \tag{4.6}$$

where C is a constant and l some characteristic turbulent length scale. The shape of this spectrum agrees fairly well with the DNS data, but it has been observed that the anisotropy of the flow and other statistics are not critically dependent on the exact form of the initial energy spectrum.

Using the spectrum defined by (4.6), it can be shown that the initial non-dimensional shear number is $SK/\varepsilon = S^*/6$ where $S^* = Sl^2/\nu$. The evolution of the flow and scalar field according to the RDT equations is completely determined through the choice of S^* and the rotation number R. Here $S^* = 108$ is taken, which implies $SK/\varepsilon = 18$ and hence, the initial value of the non-dimensional shear number in the DNS and the RDT computations are the same. After the specification of the energy spectrum, S^* and R the Fourier coefficients of the velocity and the scalar can be integrated in time and the development of the Reynolds stresses, pressure–strain correlations, scalar fluxes and scalar variances can be calculated. More details of the computational procedure are given in Appendix B.

Whereas for $Sc = 1$, computations can be simplified drastically as outlined in Appendix B, for $Sc \neq 1$, integrations in an infinite three-dimensional wavenumber space have to be carried out to obtain the scalar variance and scalar flux which makes the calculations significantly more complicated and expensive. Rogers *et al.* (1986, 1989) observed a rather small difference between turbulent scalar transport at $Sc = 0.7$ and $Sc = 1$ in their DNS of homogeneous shear flow and therefore we take $Sc = 1$ in the RDT computations instead of the value $Sc = 0.7$ which is used in the DNS.

5. Results of the DNS and RDT

In this section, the results of the DNS and the predictions of RDT are presented. The flow field is first analysed. One-point statistics and the anisotropy of the turbulence are considered and the turbulent structures are studied by means of two-point velocity correlations and visualizations. Then the turbulent transport of the scalars and the mixing time scales are investigated.

5.1. *Flow field*

5.1.1. *Development of the turbulent kinetic energy and anisotropy*

The time development of the turbulent kinetic energy for the five different rotation numbers is presented in figure 3. RDT predictions and DNS results from series A and series B, which give similar results, are displayed in the figure. Both DNS and RDT show a strong influence of rotation on the stability of the flow. In figure 4, only the DNS results of series B at $R = 0$, $-1/2$ and -1 are plotted together with exponential and linear fits. The case $R = -1/2$ is the most unstable case, in agreement with previous findings (Salhi & Cambon 1997) and the analysis presented in Appendix A. The kinetic energy has a very fast exponential growth according to figure 4 at larger St values. An exponential growth of the kinetic energy is also observed in the DNS results at $R = 0$ at larger St values, but the RDT results do not show this behaviour. Consequently, there is a discrepancy between the DNS and RDT results for $St > 6$ which also, but to a lesser extent, can be observed at $R = -1$ for $St > 8$.

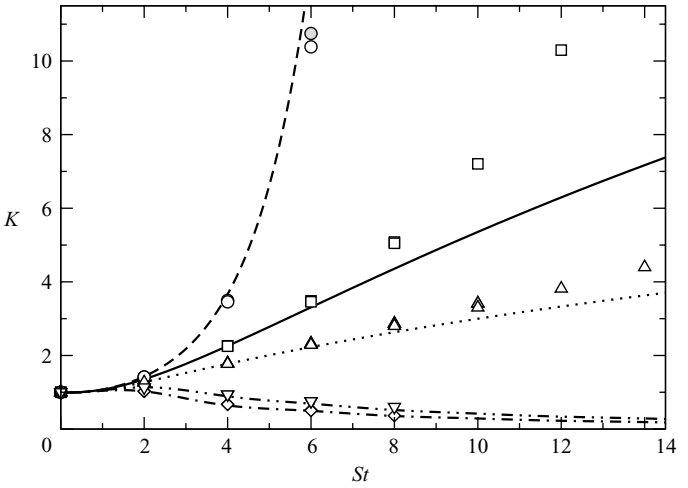

FIGURE 3. Time development of the turbulent kinetic energy K according to DNS (symbols) and RDT (lines). The time t is made non-dimensional with the shear rate S and K is scaled with its initial value. ($\triangledown$, $-\cdots-$), $R=1/2$; ($\square$, ———), $R=0$; ($\circ$, $-\ -\ -$), $R=-1/2$; ($\triangle$, $\cdots$), $R=-1$; ($\diamond$, $-\cdot-$), $R=-3/2$. The grey filled symbols are DNS results from series A and the open symbols from series B. Sometimes they are not distinguishable because the symbols overlap each other.

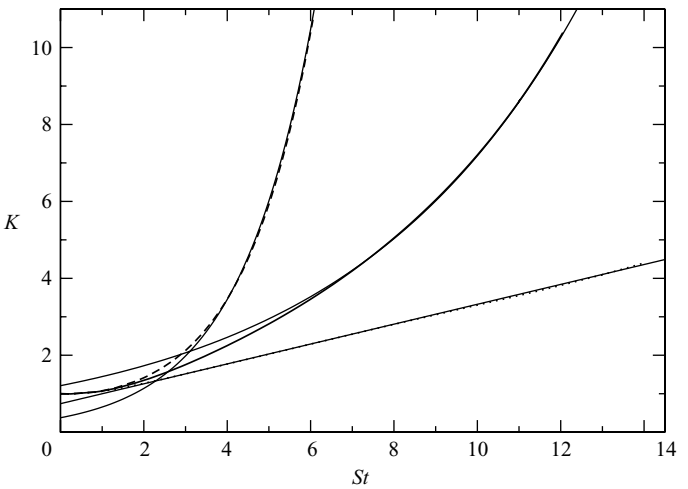

FIGURE 4. Time development of the turbulent kinetic energy K according to DNS, series B. ———, (thick line) $R=0$; $-\ -\ -$, $R=-1/2$; $\cdots$, $R=-1$. The thin solid lines are fitted exponential functions at $R=0$ ($\exp(0.178St)$) and $R=-1/2$ ($\exp(0.56St)$) and a linear fit at $R=-1$.

In the other cases, there is a reasonable to good correspondence between DNS and RDT. At $R=-1$, the kinetic energy is growing approximately linearly according the DNS, as can be seen in figure 4. Bardina *et al.* (1983) observed in their LES for $R=-1$ an approximately constant kinetic energy and this difference is likely to be a consequence of the lower non-dimensional shear number used in their study. In the other two cases, $R=-3/2$ and $R=1/2$, the kinetic energy first increases very slightly, but then decreases slowly according to DNS and RDT which implies a stabilizing

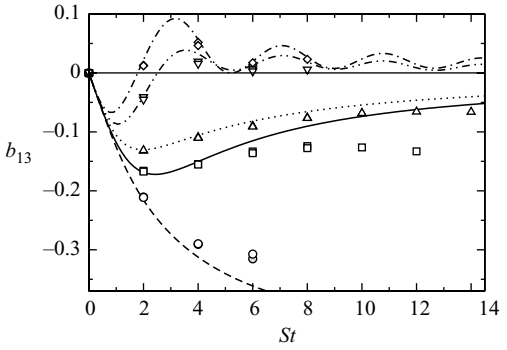

FIGURE 5. Time development of the Reynolds stress anisotropy component b_{13}. Symbols and lines as in figure 3.

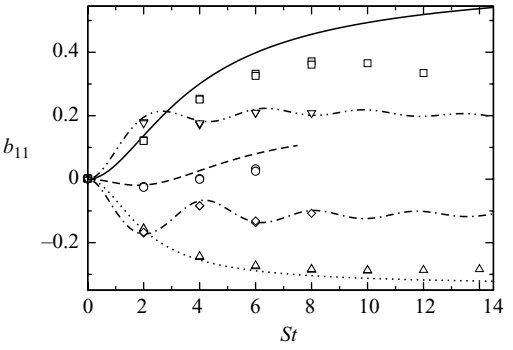

FIGURE 6. Time development of the Reynolds stress anisotropy component b_{11}. Symbols and lines as in figure 3.

influence of rotation on the turbulence (Salhi 2002). We observe also in figure 3 a clear difference between the cases R and $-1-R$, i.e. between $R=0$ and $R=-1$ and between $R=1/2$ and $R=-3/2$ caused by the influence of the pressure, confirming the analysis of Salhi & Cambon (1997).

The next point of attention is the anisotropy of the turbulence. Figure 5 shows the development of the streamwise velocity fluctuation in terms of the Reynolds stress anisotropy component b_{13} where $b_{ij}=\overline{u_iu_j}/(2K)-\delta_{ij}/3$. At $R=-1/2$, b_{13} reaches very large negative values implying a strong correlation between the streamwise and transverse velocity fluctuations. The velocity cross-correlation $\overline{u_1u_3}/u_1'u_3'$ is as large as -0.86 at $St=6$ according to the DNS. At $R=0$ and $R=-1$, b_{13} at first sharply decreases, but then increases again and it becomes approximately constant at larger St values. The DNS corresponds well to the RDT predictions until $St=4$ at $R=0$, but thereafter b_{13} is significantly more negative in the DNS. The pressureless analysis presented in Appendix A predicts oscillations of $\overline{u_1u_3}$ with a period of 3.6 at $R=-3/2$ and $R=1/2$ and this behaviour can also be observed in the DNS and RDT results. Moreover, b_{13} becomes positive according to RDT and DNS, implying an energy transfer from the turbulence to the mean flow.

Figures 6, 7 and 8 show the development of b_{11}, b_{22} and b_{33}, respectively. In the pure shear case $R=0$, the production term of $\overline{u_1u_1}$ is positive and there is no production of $\overline{u_3u_3}$. At $R=-1/2$, however, both Reynolds stresses have a positive production term

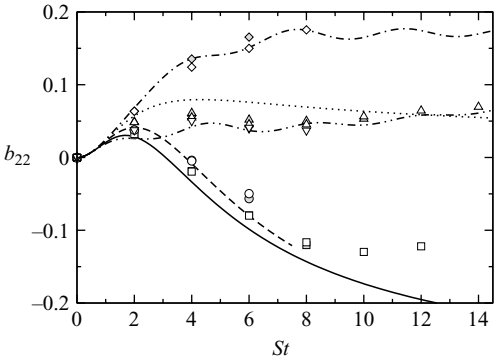

FIGURE 7. Time development of the Reynolds-stress anisotropy component b_{22}. Symbols and lines as in figure 3.

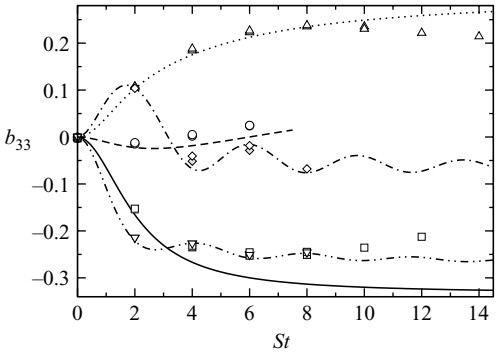

FIGURE 8. Time development of the Reynolds-stress anisotropy component b_{33}. Symbols and lines as in figure 3.

due to rotation and at $R=-1$, only $\overline{u_3u_3}$ has a production term as can be seen in (2.3) and (2.5). In accordance with this, at $R=0$, the streamwise velocity fluctuations are large and b_{11} is positive, but at $R=-1/2$, b_{11} and b_{33} are approximately equal and at $R=-1$, b_{33} is positive and b_{11} negative, signifying strong transverse and weak streamwise velocity fluctuations. RDT shows, at $R=0$, a monotic increase and decrease of b_{11} and b_{33}, respectively, but in the DNS, the nonlinear effects are strong enough to reduce the anisotropy at larger St values (figures 6 and 8) leading to significant differences with the RDT predictions. The anisotropy of the turbulence, however, is still much larger than in a homogeneous shear flow at the equilibrium state (Tavoularis & Corrsin 1981). At $R=1/2$ and $R=-3/2$, b_{11} and b_{33} follow initially the same trend as at $R=0$ and $R=-1$, respectively, but then start to oscillate with a decaying amplitude.

The spanwise velocity fluctuations are only influenced by rotation through the pressure–strain correlation and the dissipation term according to (2.4). Weak oscillations of b_{22} are observed in figure 7 at $R=1/2$ and $R=-3/2$ and negative values at $R=0$ and $R=-1/2$ at larger St values.

Similar trends regarding the anisotropy development of the turbulence at $R=0$, $-1/2$ and -1 in rotating homogeneous shear flow, but at a lower non-dimensional shear rate, have been observed by Bardina *et al.* (1983) and Salhi & Cambon (1997).

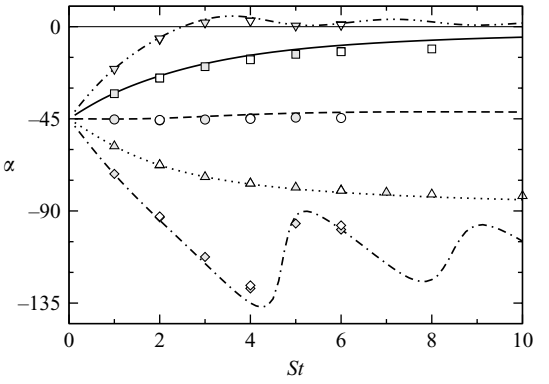

FIGURE 9. Time development of α_u. Symbols and lines as in figure 3.

In order to understand better the influence of rotation on the anisotropy of the turbulence, it is worth considering the principal angle of the Reynolds stress tensor, defined here as

$$\alpha_u = \tfrac{1}{2}\tan^{-1}[2\overline{u_1u_3}/(\overline{u_1u_1} - \overline{u_3u_3})]. \tag{5.1}$$

The definition is such that α_u is the angle of the principal axis corresponding to the largest eigenvalue, i.e. largest principal Reynolds stress, with the x_1-axis. The angles for the five cases obtained from DNS and RDT are plotted in figure 9. It can be shown that, for a positive production rate of kinetic energy, the requirement is $-90^\circ < \alpha_u < 0^\circ$. For the non-rotating case, $\alpha_u = -13^\circ$ according to the DNS at $St = 12$ compared to the value $\alpha_u = -19^\circ$ found in experiments which where conducted at a lower non-dimensional shear number (Ferchichi & Tavoularis 2002). At $R = -1/2$ and $R = -1$, α_u is very close to -45° and -90°, respectively, at larger St values which is related to a decrease of $\overline{u_1u_1}$ production and the increase of $\overline{u_3u_3}$ production owing to rotation. A simple displaced particle analysis predicts $\alpha_u = 0^\circ$, -45° and -90° for $R = 0$, $-1/2$ and -1, respectively (Tritton 1992), quite close to the DNS values. At $R = 1/2$, α_u approaches a value around 0° and at $R = -3/2$, α_u decreases below -90° and starts to oscillate.

The pressure–strain correlations are considered in order to obtain a more complete understanding of development of the turbulent anisotropy and the importance of nonlinear effects. In the following, the rapid and the slow pressure–strain correlations are denoted by Π^r_{ij} and Π^s_{ij}, respectively. The slow part of Π_{ij} is related to the nonlinear part of the source term in the Poisson equation of the pressure, and is therefore not included in the RDT. The pressure–strain correlations presented in the figures are all scaled with SK.

In figure 10, Π^r_{11} and Π^s_{11} are presented. In all cases, except at $R = -3/2$, Π^r_{11} is a sink term in the Reynolds-stress equation for $\overline{u_1u_1}$ and thus redistributes the streamwise kinetic energy to the other directions. At $R = 0$, there is a considerable difference between the RDT predictions of Π^r_{11} and the DNS results, whereas in the other cases there is a fair agreement. The DNS shows a decrease of Π^r_{11} after $St = 8$ at $R = 0$, in contrast to the RDT predictions. At $R = 0$ and $R = -1/2$, Π^s_{11} is a sink term and gives a significant contribution to the energy redistribution at larger St values. While at $R = 0$, Π^s_{11} is a sink term, it is a source term at $R = -1$. Because Π^r_{11} becomes very small at $R = -1$, the sum of the slow and rapid part of the pressure–strain correlation becomes positive at larger St values and thus the streamwise velocity fluctuations gain energy.

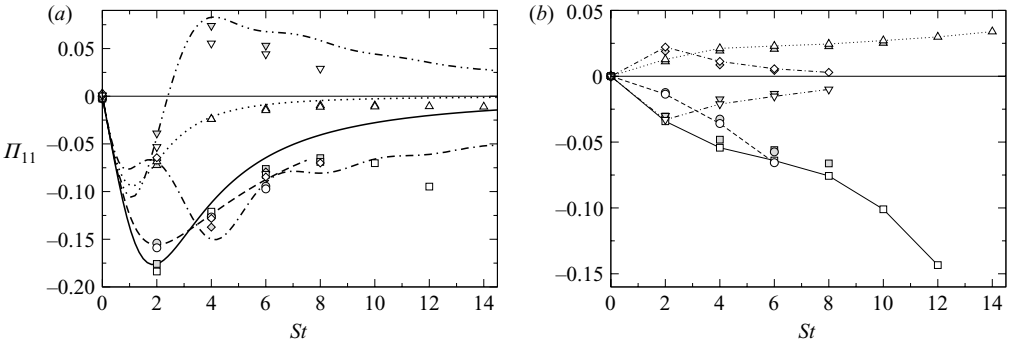

FIGURE 10. (*a*) Time development of $\Pi^r_{11}/(S\,K)$. (*b*) Time development of $\Pi^s_{11}/(S\,K)$. Only DNS data are displayed. Symbols and lines as in figure 3.

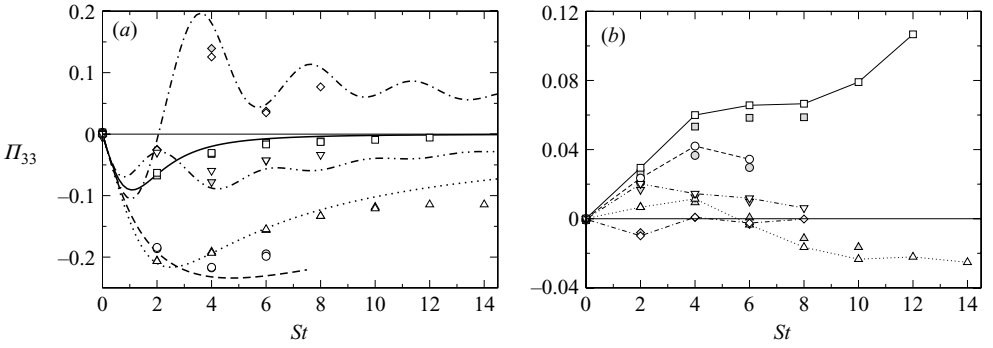

FIGURE 11. (*a*) Time development of $\Pi^r_{33}/(S\,K)$. (*b*) Time development of $\Pi^s_{33}/(S\,K)$. Only DNS data are displayed. Symbols and lines as in figure 3.

In figure 11, Π^r_{33} and Π^s_{33} are presented. At $R=-1/2$ and -1, Π^r_{33} is a large sink term, but this is opposed by a positive production term, as discussed before, and, as a result, the transverse velocity fluctuations still grow. At $R=0$, Π^s_{33} is much larger than Π^r_{33} at larger St, and the sum becomes a source term. At $R=-3/2$, Π^r_{33} becomes a source term after about $St=2$ for the transverse velocity fluctuations. This does not result in an increase of $\overline{u_3u_3}$ because after $St=2$ the production of $\overline{u_3u_3}$ becomes negative.

In figure 12, Π^r_{13} and Π^s_{13} are displayed. At $R=0$, Π^r_{13} is initially large, but then decreases rapidly whereas Π^s_{13} increases and is larger than Π^r_{13} for $St>5$. At $R=-1/2$, Π^s_{13} is also positive and gives a significant contribution at larger St values, but in the other three remaining cases, Π^s_{13} gives a very small contribution to the total pressure–strain correlation.

The RDT predictions of the development of the kinetic energy, anisotropy and pressure–strain correlations correspond well, in general, with the DNS at $R=1/2$ and $R=-3/2$. The nonlinear effects in terms of Π^s_{ij} appear to be weak in these two cases and seem to be strongly damped by the rotation. At $R=-1/2$ and $R=-1$, the nonlinear effects are noticeable, for instance in the development of the anisotropy, but the most clear nonlinear effects are observed at $R=0$, although the non-dimensional shear rate was high during the simulation period. However, a similar result was obtained by Kim (1989) who found that the slow pressure fluctuations have the same magnitude as the rapid pressure fluctuations in the rapidly sheared layer near the wall

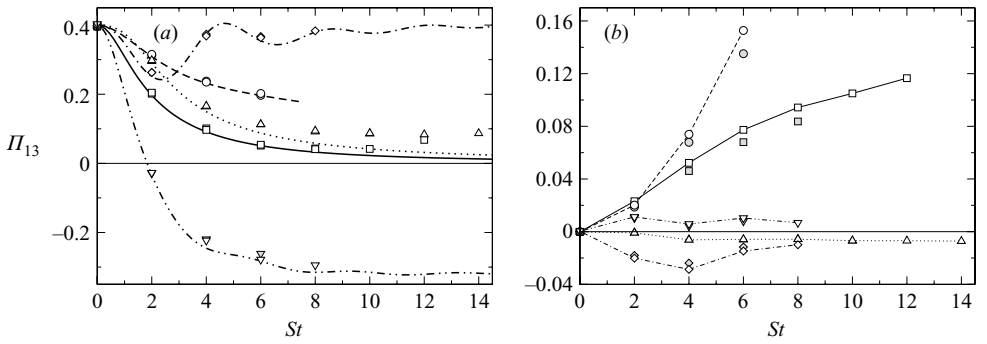

FIGURE 12. (*a*) Time development of $\Pi^r_{13}/(S\,K)$. (*b*) Time development of $\Pi^s_{13}/(S\,K)$. Only DNS data are displayed. Symbols and lines as in figure 3.

in a turbulent channel flow, contrary to common belief. In the DNS in the present study, all the slow pressure–strain correlations, except for the spanwise direction, are larger than the rapid pressure–strain correlations for $St > 7$.

In order to study the importance of the nonlinear effects on the development of the turbulence at $R = 0$ and $R = -1$ in more detail, simulations have been performed with the same initial velocity field, the same code and the same numerical parameters as the cases $R = 0$ and $R = -1$ in series B, but with the nonlinear terms explicitly set to zero. The results of this linear simulation are compared with the cases $R = 0$ and $R = -1$ in series B. The results of the linear simulation should correspond well to the RDT predictions, which they do, but we wanted to be sure to have the same influence of finite domain size, domain deformation and remeshing in the linear and nonlinear simulations. The differences between the two simulations are thus solely the result of nonlinear contributions. Although the dissipation of kinetic energy is significantly larger for $St > 6$ (figure 13*b*) owing to the nonlinear effects, the growth of K at $R = 0$ is faster in the nonlinear simulation than in the linear for $St > 6$ because of a larger production term, as will be discussed later. The growth of K at $R = 0$ in the nonlinear simulation at larger St values can be approximated by $\exp(0.178\,St)$, whereas in the linear simulations it is approximately linear. The growth rate at $R = 0$ in the DNS, which is at $St = 12$ still far from equilibrium conditions, is faster than in the experiments close to equilibrium conditions of Tavoularis & Corrsin (1981). In the latter study, the growth rate can be approximated by $\exp(0.122\,St)$ when the centreline mean velocity in the experiments is taken as the advection velocity. Rogers (1991) proves that, in the long time limit, K grows linearly in a non-viscous RDT at $R = 0$. In a viscous RDT, as in the present study, the growth rate is less than linear at large times, but up to $St = 12$ it is close to linear in the linear simulation presented in figure 13. At $R = -1$, the differences between the linear and nonlinear simulations are not as large, but also in this case, K is larger in the nonlinear simulations at larger St values.

The largest difference between the nonlinear and linear simulation at $R = 0$ occurs in the development of $\overline{u_3 u_3}$, which is presented in figure 14(*a*). According to non-viscous RDT (Rogers 1991) and viscous RDT, $\overline{u_3 u_3}$ decays monotonically at $R = 0$ and this happens also in the linear simulation. In the nonlinear DNS, however, $\overline{u_3 u_3}$ grows for $St > 3$ and at $St = 12$ there is a large difference between $\overline{u_3 u_3}$, a factor of 20, in the linear and nonlinear simulation. Already in an early stage of the simulations, at $St = 3$, a difference between the linear and nonlinear simulation can be seen, which is surprising in view of the high shear rate. The difference between the development

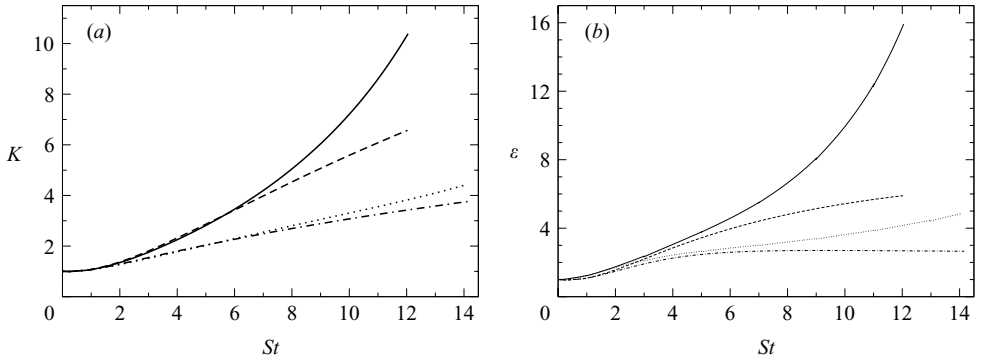

FIGURE 13. Time development of (*a*) K and (*b*) ε at $R=0$ series B (———) and $R=-1$ series B ($\cdots$) and the corresponding simulations without the nonlinear terms at $R=0$ (– – –) and at $R=-1$ (– · –).

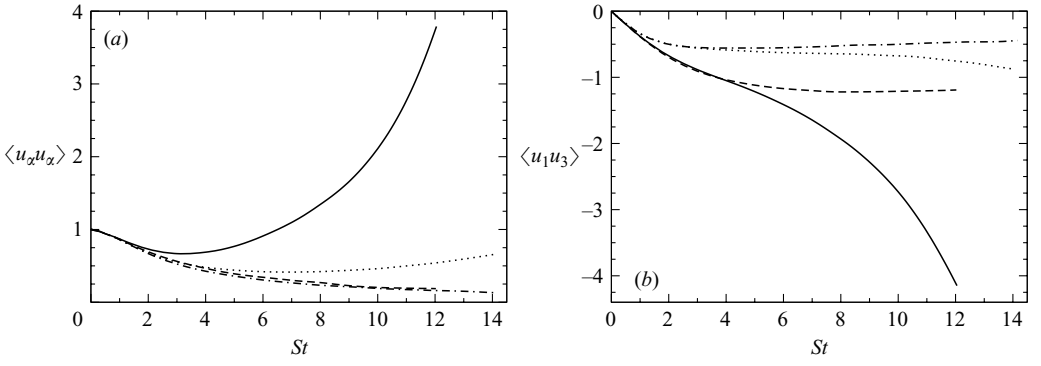

FIGURE 14. Time development of (*a*) $\overline{u_3u_3}$ at $R=0$ and $\overline{u_1u_1}$ at $R=-1$ and (*b*) $\overline{u_1u_3}$ at $R=0$ and $R=-1$ in the linear and nonlinear simulation. Lines as in figure 13.

of $\overline{u_3u_3}$ in the linear and nonlinear simulation is a consequence of Π^s_{33} which gives a positive contribution to the growth of the transverse velocity fluctuations, as has been shown in figure 11. At $R=-1$, $\overline{u_1u_1}$ grows for $St>7$ in the nonlinear simulation, whereas in the linear simulation, it monotonically decays. At $St=14$, $\overline{u_1u_1}$ it is almost a factor of 5 larger in the nonlinear simulation. In this case, the difference is due to the positive contribution of Π^s_{11} to the growth of the velocity fluctuations.

Figure 14(*b*) presents the development of $\overline{u_1u_3}$ in the linear and nonlinear simulation. Rogers has proved that $\overline{u_1u_3}$ becomes constant in a non-viscous RDT at large times at $R=0$. Non-viscous RDT computations strongly indicate the same asymptotic behaviour of $\overline{u_1u_3}$ at $R=-1$, but, in a viscous RDT, $\overline{u_1u_3}$ decays at large times. In figure 14(*b*) we can observe a growing discrepancy between the linear and nonlinear simulation for $St>4$. At the end of the simulations at $R=0$ and $R=-1$, $\overline{u_1u_3}$ is larger in the nonlinear simulation than in the linear simulation and this explains the faster growth of the kinetic energy in the nonlinear DNS. The reason for the larger magnitude of $\overline{u_1u_3}$ is not due to Π^s_{13} because at $R=0$ it opposes the development of negative $\overline{u_1u_3}$ correlations and at $R=-1$ it is very small, but it is the larger $\overline{u_3u_3}$ and $\overline{u_1u_1}$ correlation in the nonlinear simulations at $R=0$ and $R=-1$, respectively.

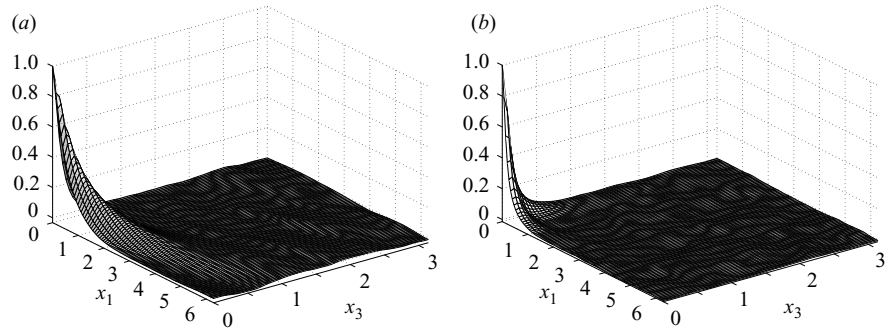

FIGURE 15. The two-point correlations (*a*) $\rho[u_1](\boldsymbol{r})$ and (*b*) $\rho[u_3](\boldsymbol{r})$ at $R=0$ and $St=12$, series *B*, for separation vectors in the (x_1, x_3)-plane. Here, u_1 is almost parallel to the principal axis of the Reynolds stress tensor and u_3 perpendicular.

5.1.2. *Turbulent structures*

It is known that a high shear rate causes elongated streamwise structures in homogeneous shear flow which bear close similarities with the structures encountered in wall-bounded shear flows (Lee *et al.* 1990). Quantitative information about turbulent length scales can be obtained from two-point velocity correlations (no summation of repeated indices)

$$\rho[u_i](\boldsymbol{r}) = \overline{u_i(\boldsymbol{x})u_i(\boldsymbol{x}+\boldsymbol{r})}/\,\overline{u_i u_i}. \tag{5.2}$$

Two-point velocity correlations with the separation distance vector $\boldsymbol{r}$ in the (x_1, x_3)-plane have been extracted from the DNS at different rotation numbers and at the end of the simulations so that the elongation of the structures is most pronounced. Figure 15(*a*) presents $\rho[u_1](\boldsymbol{r})$ at $R=0$, figure 16(*a*) presents $\rho[u_i](\boldsymbol{r})$ at $R=-1/2$ where u_i is the velocity component in the (x_1, x_3)-plane with an angle of -45° to the flow direction and figure 17(*a*) presents $\rho[u_3](\boldsymbol{r})$ at $R=-1$. These velocity components are all approximately parallel to the principal axis of the Reynolds stress tensor corresponding to the Reynolds stress with the highest fluctuation intensity. The direction of this particular principal axis has been displayed in figure 9. The figures show the typical long correlation length in a direction almost parallel to the flow direction of these velocity components parallel or almost parallel to the principal axis of the Reynolds stress tensor. A closer examination reveals that the longest correlation length appears at an angle of approximately 10° with the flow direction, with little variation of the angle at different rotation numbers.

Figure 15(*b*) presents $\rho[u_3](\boldsymbol{r})$ at $R=0$, figure 16(*b*) presents $\rho[u_i](\boldsymbol{r})$ at $R=-1/2$ where u_i is the velocity component in the (x_1, x_3)-plane with an angle of 45° to the flow direction and figure 17(*b*) presents $\rho[u_1](\boldsymbol{r})$ at $R=-1$. These velocity components are perpendicular to the velocity components whose two-point correlations are plotted in figure 15(*a*), 16(*a*) and 17(*a*), respectively. They are thus almost parallel to the principal axis of the Reynolds stress tensor corresponding to the Reynolds stress with the lowest fluctuation intensity. The velocity components in this direction have a much shorter correlation length, as can be seen in figures 15(*b*), 16(*b*) and 17(*b*). At $R=0$, $-1/2$ and -1, the velocity components with a high turbulence intensity have thus a long correlation length and the velocity components with a low turbulence intensity have a short correlation length.

RDT significantly underpredicted the intensity of the transverse velocity fluctuations at $R=0$ and the streamwise velocity fluctuations at $R=-1$ because there was a

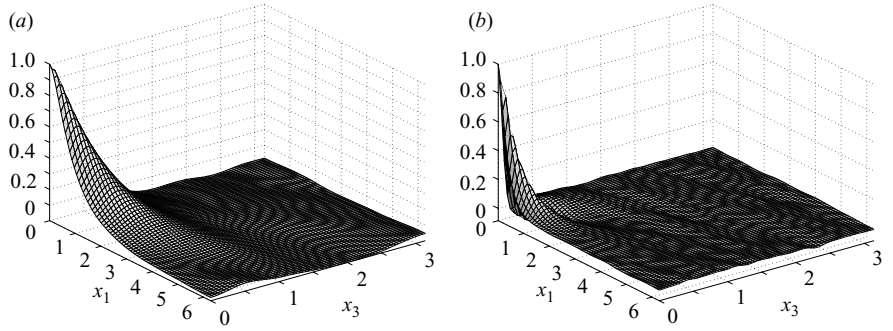

FIGURE 16. The two-point correlations (*a*) $\rho[u](\boldsymbol{r})$ and (*b*) $\rho[w](\boldsymbol{r})$ at $R=-1/2$ and $St=6$, series *A*, for separation vectors in the (x_1, x_3)-plane. Here, $u=u_1\cos\alpha_u+u_3\sin\alpha_u$, $w=-u_1\sin\alpha_u+u_3\cos\alpha_u$ and $\alpha_u=-45^\circ$. Thus, u is the strongest fluctuating velocity component and is parallel to the principal axis of the Reynolds stress tensor and w perpendicular.

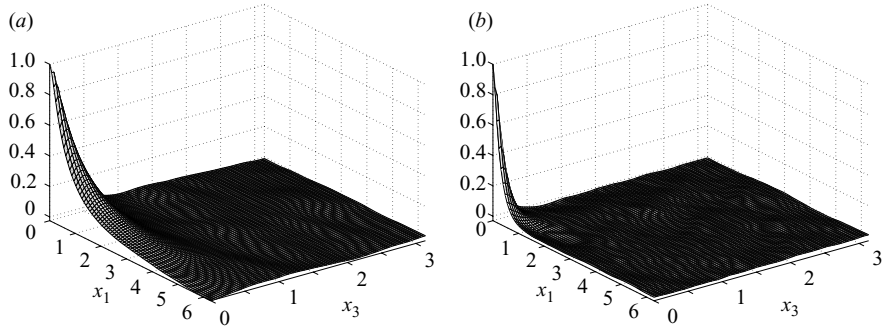

FIGURE 17. The two-point correlations (*a*) $\rho[u_3](\boldsymbol{r})$ and (*b*) $\rho[u_1](\boldsymbol{r})$ at $R=-1$ and $St=14$, series *B*, for separation vectors in the (x_1, x_3)-plane. Here, u_3 is almost parallel to the principal axis of the Reynolds stress tensor and u_1 is perpendicular.

considerable energy transfer owing to the slow pressure–strain correlations as we have observed before. In these cases, RDT overpredicts the correlation length in comparison with the DNS (results are omitted here). This shows that, in the DNS, mainly the transverse velocity fluctuations with higher wavenumbers at $R=0$ and the streamwise velocity fluctuations with higher wavenumbers at $R=-1$ gain energy by nonlinear processes, which leads to shorter correlation lengths than in the RDT simulations.

In the two stabilized cases, $R=-3/2$ and $R=1/2$, the two-point velocity correlations do not reveal clear elongated structures in the flow direction and are therefore not presented here.

According to the two-point velocity correlation, we might expect to see streaky velocity structures at $R=0$, $R=-1/2$ and $R=-1$. These are indeed observed in instantaneous plots of the fluctuating velocity presented in figure 18(a, b, c) in a plane, with an angle of 10° to the flow direction. In the plots, elongated turbulent structures in the flow direction can be observed of low- and high-speed flow. Note that at $R=0$, an instantaneous plot of the streamwise fluctuating velocity is shown, but at $R=-1/2$ and $R=-1$, an instantaneous plot of u (see the caption of figure 16 for the definition) and the transverse fluctuating velocity is shown, respectively. At $R=-1$, an instantaneous plot of the streamwise fluctuating velocity does not show

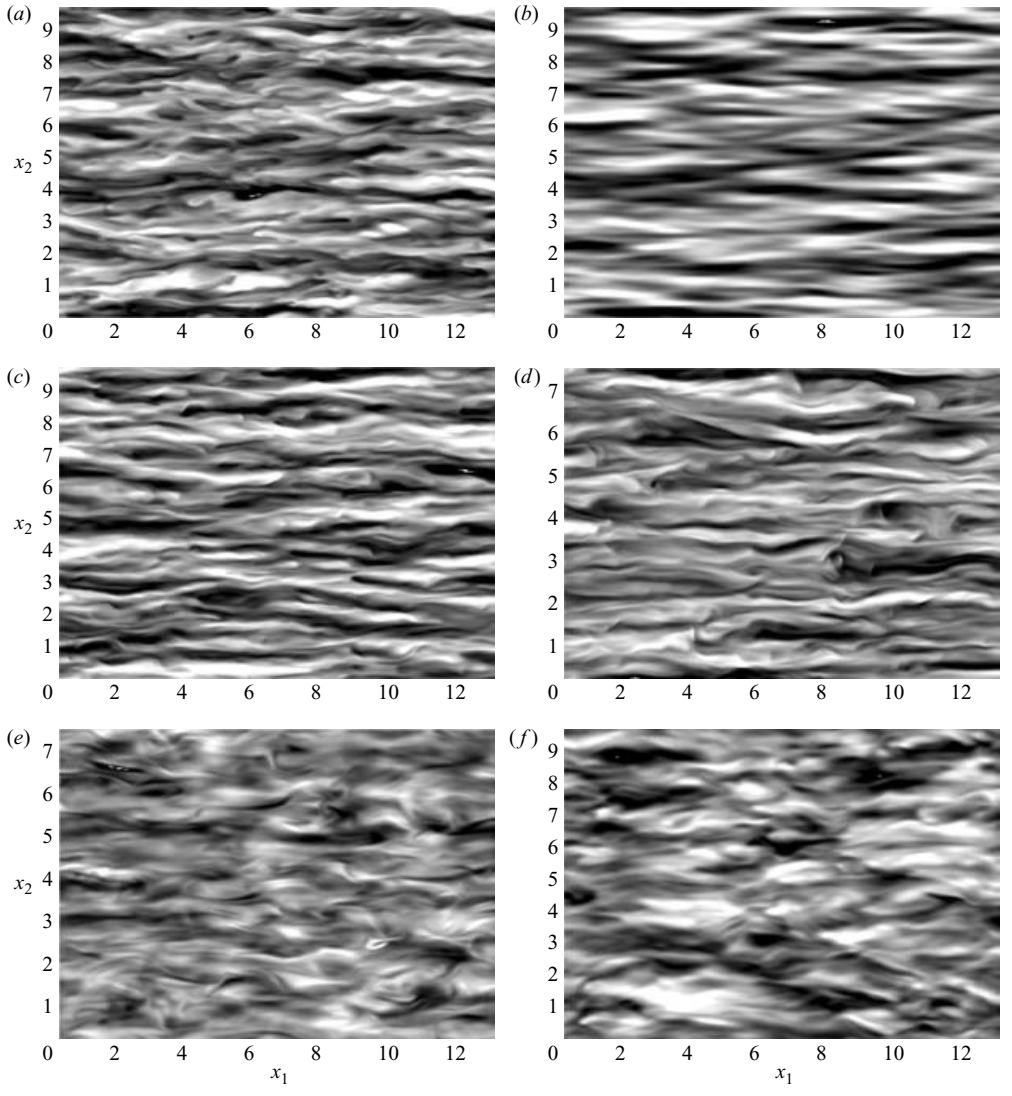

FIGURE 18. The instantaneous velocity in a (x, x_2)-plane where x is at 10° to the flow direction. (*a*) Streamwise velocity at $R = 0$ and $St = 8$; (*b*) streamwise velocity at $R = 0$ and $St = 8$ for the RDT (the other plots are all obtained from DNS); (*c*) velocity component u (see the caption of figure 16 for the definition of u) at $R = -1/2$ and $St = 6$; (*d*) transverse velocity at $R = -1$ and $St = 10$; (*e*) transverse velocity at $R = -3/2$ and $St = 6$; (*f*) streamwise velocity at $R = 1/2$ and $St = 6$.

any streaky structures, as can be expected from the two-point correlation presented in figure 17.

The turbulent structures found at $R = 0$ are similar to the structures observed by Lee *et al.* (1990) in a rapidly sheared non-rotating homogeneous shear flow. Lee *et al.* remarked that these structures resemble the streaky streamwise structures in the near-wall region of a turbulent channel flow. We have also performed a simulation with the same parameters and initial velocity field as the $R = 0$ case, but without the nonlinear terms. This simulation thus represents a RDT calculation, and a plot of the streamwise velocity fluctuations is shown in figure 18(*b*). Streamwise streaks are also observable

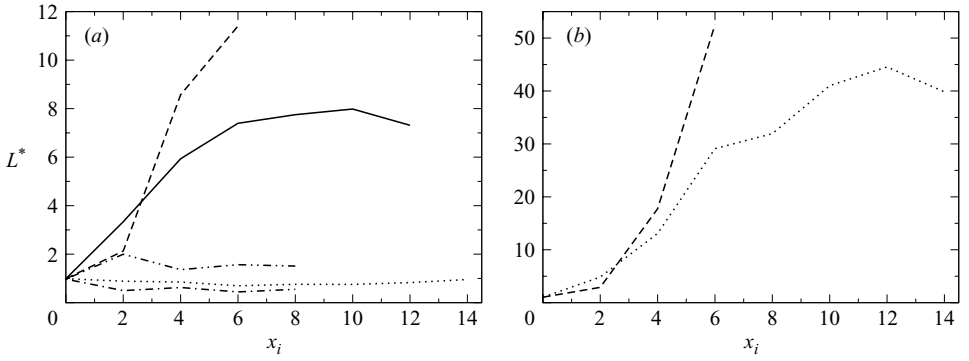

FIGURE 19. The elongation parameter for the streamwise velocity component (a) and for the transverse velocity component (b). (——), $R = 0$; (— — —), $R = -1/2$; (· · ·), $R = -1$; (— · · —), $R = 1/2$; (— · —), $R = -3/2$.

in this case which shows that linear processes can generate the streaks, an observation that is in agreement with Kim & Lim (2000), but the velocity field is much smoother than in the case with the nonlinear terms included (see figure 18a) because the small scales do not gain energy by nonlinear instabilities and are damped by viscous effects.

Alvelius & Johansson (1999) performed DNS of turbulent channel flow with spanwise rotation. In the simulations, there was a large region in the middle of the channel where the absolute mean vorticity was approximately zero which corresponds to the $R = -1$ case considered here. Alvelius & Johansson observed long streamwise structures with a positive wall-normal velocity in this middle region of the rotating channel flow. This observation corresponds well with the results shown in figure 18(d).

Figures 18(e) and 18(f) present instantaneous plots of the transverse and streamwise fluctuating velocity at $R = -3/2$ and $R = 1/2$, respectively, in a plane with an angle of 10° to the flow direction. These velocity components are also approximately aligned with the principal axis of the Reynolds stress tensor. At $R = 1/2$, the instantaneous streamwise velocity structures are somewhat stretched in the flow direction, but there are no distinctive elongated structures such as in the cases $R = 0$, $R = -1/2$ and $R = -1$. Turbulent structures are even less clear at $R = -3/2$. The most coherent large-scale turbulent structures in our study are thus found in the cases where the kinetic energy is growing.

To quantify the formation of streaky structures in homogeneous shear flows, Lee *et al.* (1990) and Salhi & Cambon (1997) used the eddy elongation parameter $L^* = \ell_1/\ell_2$. In the case of the streamwise velocity fluctuations, we use $\ell_1 = L_1^1$ and $\ell_2 = 2L_1^2$ for the streamwise and spanwise length scales, respectively, similar to Lee *et al.* (1990). The length scales are obtained by integrating the two-point correlations (5.2)

$$L_j^i = \int_0^\infty \rho[u_j](\boldsymbol{r} + x\boldsymbol{e}_i)\,\mathrm{d}x. \tag{5.3}$$

Lee *et al.* suggested $L^* > 8$ as the criterion for streaky structures.

Figure 19(a) shows L^* extracted from the DNS at the different rotation numbers. Analytical expressions for L^* obtained from inviscid RDT are presented by Salhi & Cambon (1997). At $R = 0$, L^* seems to approach an asymptotic value close to the criterion for streaky structures, whereas in RDT, L^* monotonically increases (Salhi & Cambon). An explanation is the decrease of L_1^2 in the RDT, whereas in the DNS it is approximately constant after some time. The streak spacing or L_1^2 in the DNS seems

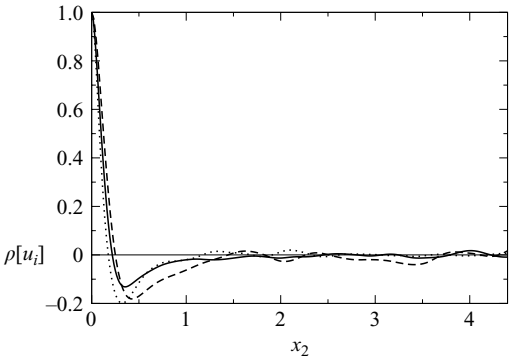

FIGURE 20. Two-point velocity correlations: (———), $\rho[u_1](x_2)$ at $R=0$ and $St=12$, series B; (− − −), $\rho[u](x_2)$ at $R=-1/2$ and $St=6$, series A (see the caption of figure 16 for the definition of u); (· · · · ·), $\rho[u_3](x_2)$ at $R=-1$ and $St=14$, series B.

to be determined by $(\nu/S)^{1/2}$ as discussed here in after, but in the RDT, this is not the case. Kim & Lim (2000) concluded from numerical experiments of turbulent channel flow that the nonlinear terms are necessary to produce the proper streak spacing and this conclusion seems to be confirmed by the present simulations. At $R=-1/2$, L^* grows faster than at $R=0$, but at $R=1/2$, -1 and $-3/2$, L^* stays approximately constant or oscillates weakly showing the absence of streaky structures. Similar results are obtained by RDT as shown by Salhi & Cambon (1997).

In figure 19(b), we present $L^*=\ell_1/\ell_2$ where $\ell_1=L_3^1$ and $\ell_2=L_3^2$, i.e. the integral length scales for the transverse velocity component, extracted from the DNS at $R=-1/2$ and -1. (L^* is always defined so that $L^*=1$ in isotropic turbulence). In both these cases, L^* becomes very large, revealing strong elongation of the structures in the streamwise direction.

Elongated streaks of alternating high- and low-speed flow give rise to negative values of the spanwise two-point correlations. The spanwise two-point velocity correlations are plotted in figure 20 for the cases and velocity components where we can observe clear streaks, e.g. $R=0$, $R=-1/2$ and $R=-1$. The mean spacing Λ between two high-speed or low-speed streaks is about twice the separation at which the minimum value of $\rho[u_i](x_2)$ occurs. If the streak spacing is scaled with the viscous length scale $(\nu/S)^{1/2}$, we find $\Lambda=87$ at $R=0$ and $St=12$, $\Lambda=89$ at $R=-1/2$ and $St=6$, and $\Lambda=80$ at $R=-1$ and $St=14$. These values correspond reasonably well with the mean streak spacing of $\Lambda=112$ found in DNS of turbulent channel flow (Moser *et al.* 1999).

5.1.3. *Vorticity structures*

Rotation affects the small scales of the turbulence as we can see in (2.9) for the vorticity. The influence of vorticity on the small scales and in particular on vortices is studied in this section.

In table 2, the values of the anisotropy tensor components of the mean vorticity fluctuations (thus without the mean vorticity component)

$$v_{ij}=\frac{\langle\omega_i\omega_j\rangle}{\langle\omega_k\omega_k\rangle}-\tfrac{1}{3}\delta_{ij}, \tag{5.4}$$

extracted from the DNS, are given for the different rotation numbers. According to the table, v_{22} is the largest component at $R=0$, but it is not much larger than the other components. At $R=-1/2$, v_{11} is the dominating component and this is even

$R=2\Omega/S$	St	v_{11}	v_{22}	v_{33}	v_{13}
1/2	6	0.151	0.076	−0.227	0.117
0	8	−0.019	0.084	−0.064	0.111
−1/2	6	0.249	−0.156	−0.093	0.267
−1	10	0.542	−0.277	−0.265	0.167
−3/2	6	0.466	−0.187	−0.279	0.125

TABLE 2. The components of the anisotropy tensor of the vorticity fluctuations at different rotation numbers, extracted from series *A*.

more pronounced at $R=-1$ where the vorticity fluctuations of ω_2 and ω_3 are much smaller than of ω_1. This can be understood if we consider the linearized form of the vorticity equation, (2.9). At $R=-1$, linear inviscid theory shows that ω_2 and ω_3 stay constant and $\omega_1 \sim St$ because of amplification by mean shear (Cambon *et al.* 1994). The linear production appears, in fact, to be dominant at $R=-1$ (results are not presented here).

Figure 21 presents joint probability density functions (PDFs) of the strain rate $(2s_{ij}s_{ij})^{1/2}$ and the norm of the vorticity $(\omega_i\omega_i)^{1/2}$ obtained from the DNS whereby now the mean vorticity is included in ω_2 and the mean strain rate is included in s_{13}. Points close to the line $s=\omega$ correspond typically to vortex sheets, but also the mean flow gives $s=\omega$.

The joint PDF obtained from the DNS at $R=0$ and at $St=8$, displayed in figure 21(*a*), shows a high probability around the line $s=\omega$, suggesting vortex sheet behaviour, especially at large values of strain and vorticity. At the same time, there are regions in the flow with high vorticity and low strain which typically are related to vortices, and regions with high strain and low vorticity related to irrotational straining (Chong *et al.* 1998). This is even more pronounced at $St=12$ where more regions are found with high vorticity or high strain (figure 21*b*). Results are omitted here, but in a simulation without the nonlinear terms and $R=0$, regions with either large strain or large vorticity are absent.

When the rotation number decreases from $R=0$ to $-1/2$ and to -1, the vortex sheet behaviour becomes less appearant according to figure 21(*a*, *c*, *d*). The probability of strain- or vorticity-dominated regions in the flow is large at $R=-1/2$. The appearance of vorticity-dominated regions, with sometimes extreme values of vorticity, is even more likely at $R=-1$, which indicates the presence of many relatively strong vortices.

At $R=-3/2$, fewer strain- or vorticity-dominated regions appear than in the former three nonlinear cases according to figure 21(*e*). The strain and vorticity are mostly of the same order, indicating the presence of vortex sheets. Similar conclusions can be drawn for the case $R=1/2$. The appearance of fewer strain- and vorticity-dominated regions is probably related to the less intensive nonlinear processes in these two cases.

Further insight into the features of the vorticity field can be obtained by using three-dimensional visualizations of vortex structures. There exist a number of techniques to identify vortices. We have applied a technique proposed by Zhou *et al.* (1999) and use the imaginary part of the complex eigenvalue of the velocity gradient tensor λ_{ci} to identify the vortices. This quantity is related to the strength of the local swirling motion of the velocity field. For instance, it is zero at places where the velocity field is not locally circular or swirling, as, for example, in vortex sheets. In the visualizations presented here, we show isosurfaces of the imaginary part of the complex eigenvalue of the velocity gradient tensor. This means that only vortices with a swirling strength

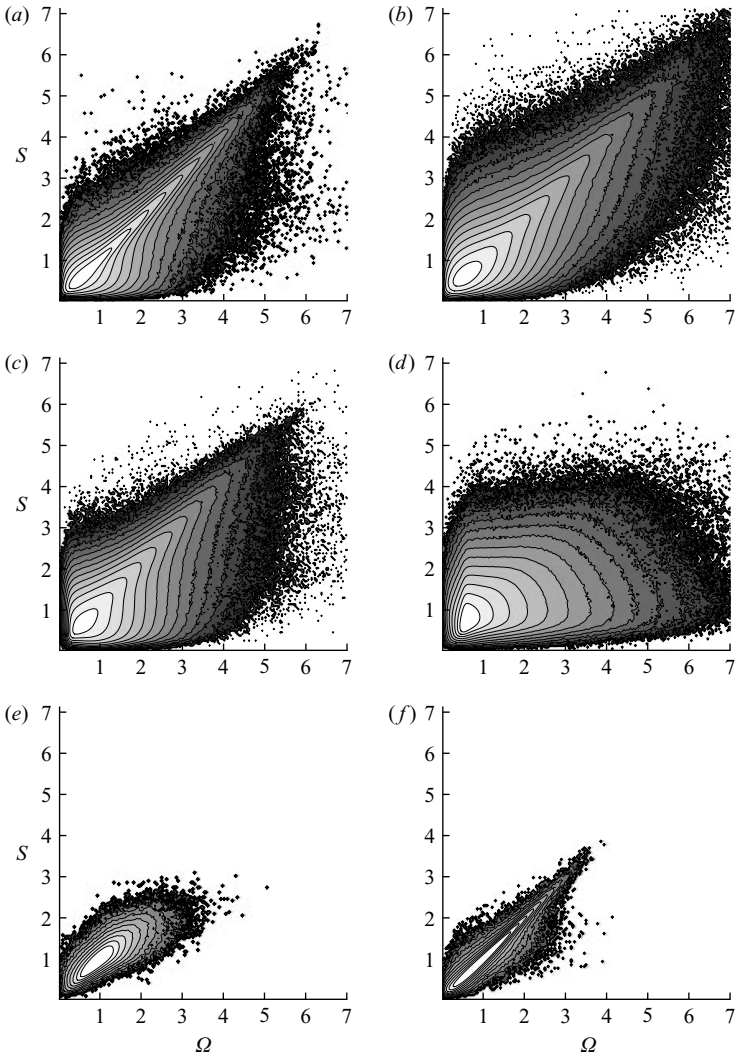

FIGURE 21. The joint PDF of the norm of the vorticity including the mean vorticity $(\omega_i\omega_i)^{1/2}$ (horizontal axis) and the strain $(2s_{ij}s_{ij})^{1/2}$ (vertical axis) whereby both are scaled with the r.m.s. of the vorticity. The difference between each contour level is one decade and a lighter shade corresponds to a higher probability. (*a*) $R=0$ and $St=8$; (*b*) $R=0$ and $St=12$; (*c*) $R=-1/2$ and $St=6$; (*d*) $R=-1$ and $St=14$; (*e*) $R=-3/2$ and $St=6$; (*f*) $R=1/2$ and $St=6$.

above a certain threshold value are visualized and vortex sheets or shear layers are not visible in the figures.

The three-dimensional visualizations presented in figure 22 show the vortical structures developed in the DNS. Many elongated quasi-streamwise vortices can be observed in figure 22(*a*) at $R=0$ and $St=8$ which are approximately aligned with the streaky structures observed in figure 18(*b*). Kim & Lim (2000) observed that in wall-bounded shear flows, linear processes can produce streaks, but the nonlinear terms are essential for the formation of the streamwise vortices. In a simulation without the nonlinear terms, we could observe streamwise vortices, but these were much weaker than in the simulation with the nonlinear terms. Apart from the

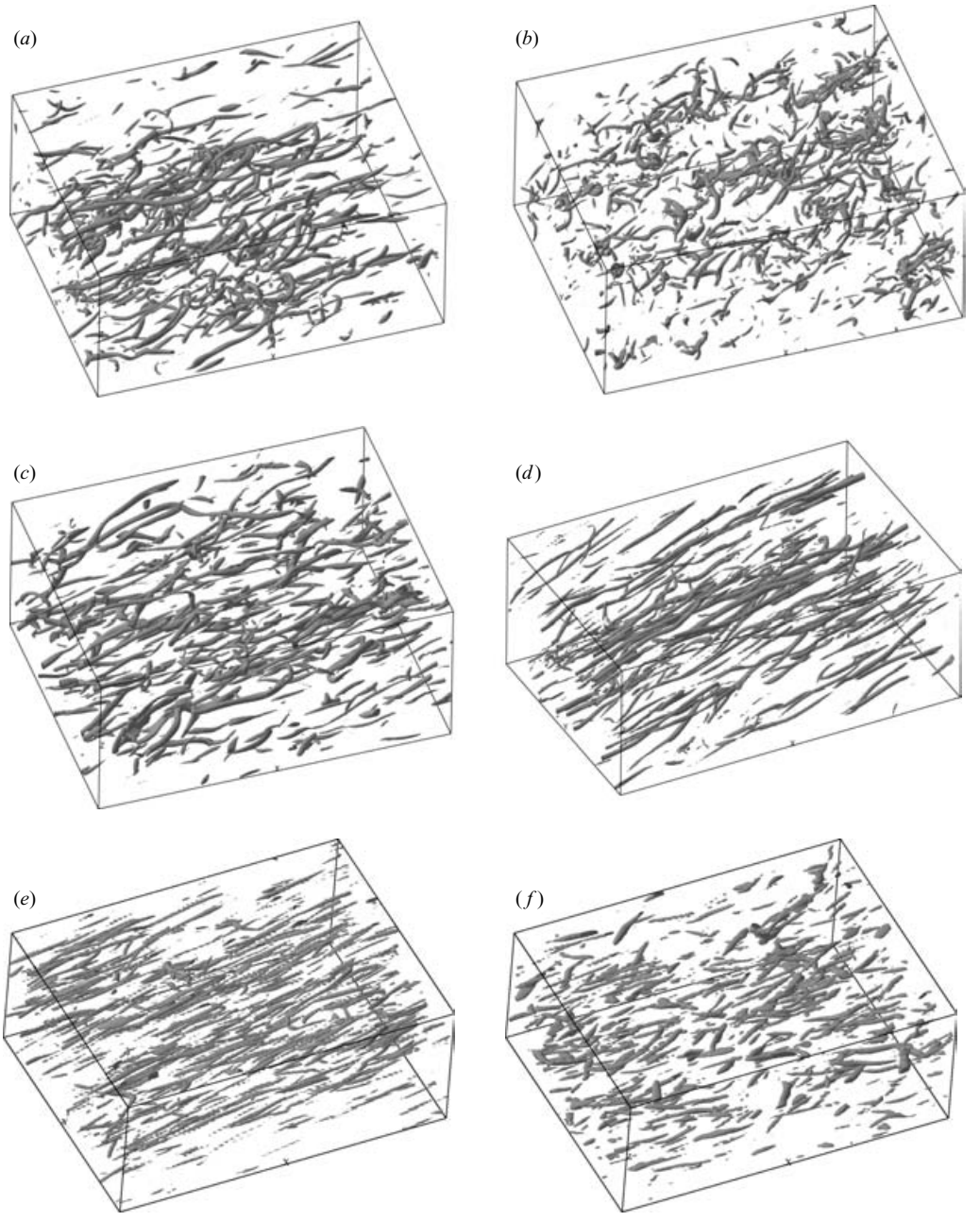

FIGURE 22. Vortices identified by isosurfaces of $|\lambda_{ci}|$ in a domain of size $L_{x_1} \times L_{x_2} \times L_{x_3} = 1.5\pi \times 1\pi \times 0.5\pi$ (a, b, c, d). $L_{x_1} \times L_{x_2} \times L_{x_3} = 2\pi \times 1.5\pi \times 0.8\pi$ (e, f). (a) $R = 0$ and $St = 8$, $|\lambda_{ci}|/S = 1.68$; (b) $R = 0$ and $St = 12$, $|\lambda_{ci}|/S = 2.75$; (c) $R = -1/2$ and $St = 6$, $|\lambda_{ci}|/S = 1.40$; (d) $R = -1$ and $St = 14$, $|\lambda_{ci}|/S = 2.07$; (e) $R = -3/2$ and $St = 6$, $|\lambda_{ci}|/S = 0.66$; (f) $R = 1/2$ and $St = 6$, $|\lambda_{ci}|/S = 0.48$.

streamwise vortices, some hairpin-like vortical structures can be distinguished in figure 22(a) and many short curved vortex tubes can be seen, which are more or less aligned with the spanwise direction. These latter structures could well be parts or remains of hairpin vortices. The vorticity field has a quite different appearance at a

later stage in the DNS at $St = 12$ when the nonlinear processes are much stronger, as shown in figure 22(*b*). There are some streamwise vortices, but they are not as long and pronounced as at $St = 8$. Instead many relative short vortex tubes can be observed with a more isotropic orientation or with a spanwise orientation. These observations show similarities with the observations of Kida & Tanaka (1994) who also found that the streamwise vortices disappear and the vorticity field becomes more isotropic at larger St values in homogeneous shear flow.

Streamwise and spanwise vortex tubes and hairpin-like vortical structures have also been observed by Rogers & Moin (1987) and Kida & Tanaka (1994) in non-rotating homogeneous shear flows, but at much lower shear rates. The latter argued that the spanwise vortex tubes are a consequence of a rolling up of vortex sheets through the Kelvin–Helmholtz instability. This is, however, a linear instability process and we would therefore expect to see these spanwise vortex tubes in a simulation without the nonlinear terms, if this linear instability mechanism exists, but they are absent in the simulation without the nonlinear terms at $R = 0$. The spanwise vortical structures in the DNS are thus more probably related to nonlinear processes.

In the most unstable case at $R = -1/2$ there exist many and intense streamwise vortices, as can be observed in figure 22(*c*). They have a slightly steeper angle to the flow direction, approximately 18°, than the streamwise vortices at $R = 0$. A few hairpin-like vortical structures can be observed at $R = -1/2$ and many curved vortices as well as quasi-spanwise vortices. Very elongated and intense streamwise vortex tubes are observed at $R = -1$ in figure 22(*d*). Similar structures were observed by Tanaka *et al.* (1998) in rotating homogeneous shear flow at $R = -1$ at a lower shear rate. The dominance of the streamwise vortices at $R = -1$ was already indicated by the vorticity anisotropy tensor presented in table 2. To a smaller extent, spanwise vortex tubes can be observed, and streamwise vortex tubes with a hook-like shape at one of the ends resembling one-sided hairpin vortical structures.

Much weaker and less distinct streamwise vortex structures are observed in the stabilized case $R = -3/2$ displayed in figure 22(*e*), but the predominance of streamwise oriented vortex tubes is still obvious. Vortices appear to be even weaker at $R = 1/2$ which is indicated by the low value of $|\lambda_{ci}|$ used in figure 22(*f*) to visualize the vortices. At $R = 1/2$, most of the vortices are not lying in a (x_1, x_3)-plane as in the other cases, but have a component in the spanwise direction. Owing to the strong shear, they still have a small angle with the flow direction. Besides these vortices, also quite thick and short vortical structures can be observed with a spanwise orientation. Hairpin-like vortical structures seem to be absent in both stabilized cases.

The presence of streamwise vortices is a common feature at $R = -1/2$, -1 and 0 in the DNS. The swirling motion of fluid particles in the streamwise vortices is, however, quite different at the different rotation numbers. To study this topic in more detail, a useful quantity is the relative helicity density fluctuation, which is defined as

$$h' = \frac{\boldsymbol{u} \cdot \boldsymbol{\omega}}{|\boldsymbol{u}|\ |\boldsymbol{\omega}|} = \cos\phi, \tag{5.5}$$

where ϕ is the angle between the velocity and vorticity vector. Here, the mean vorticity is included in $\boldsymbol{\omega}$. The condition $\omega_1 > 1.5\,\omega'$ is used, where ω' is the r.m.s. of the vorticity, to identify mainly streamwise vortices in the DNS, otherwise the interpretation of the results will be complicated. The condition $\omega_1 > 1.5\,\omega'$ eliminates the tracing of vortex sheets and the heads of hairpin vortices because they have, in general, a relatively small streamwise vorticity component. This condition is satisfied in about 1.5 % to

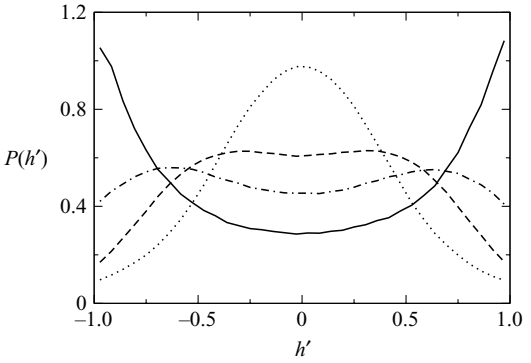

FIGURE 23. PDFs of the fluctuating relative helicity density h' conditioned on high streamwise vorticity: ———, $R=0$ and $St=8$; — · —, $R=0$ and $St=12$; — — —, $R=-1/2$ and $St=6$; · · ·, $R=-1$ and $St=14$.

2.5 % of the flow field, and visualizations show that this condition indeed traces many of the streamwise vortices.

Figure 23 presents the probability density functions (PDFs) of h' extracted from the DNS at $R=0$, $-1/2$ and -1 for the regions of the flow field where the condition $\omega_1 > \beta\,\omega'$ with $\beta=1.5$ is satisfied. The conditioned PDFs appear to be insensitive to the exact value of the threshold value β. The figure shows that there is a clear difference between the conditioned PDFs at different rotation numbers. At $R=0$ and $St=8$, the PDF has peaks at $h'=\pm1$, which indicates that, in many streamwise vortices, the fluid particles undergo a swirling helical motion with a large streamwise component. This is probably the reason that the streamwise velocity has a long correlation length and has a streak-like structure at $R=0$. At $St=12$, the peaks at $h'=\pm1$ have disappeared, which is probably related to the more isotropic character of the vortices at larger St values, but the high probability of large negative or positive values of h' still remains.

At $R=-1/2$, the fluid particles undergo a swirling motion with a smaller streamwise component than at $R=0$, which is indicated by the flat distribution in the PDF in the range $h'=\pm0.3$. The conditioned PDF at $R=-1$ has a peak at $h'=0$ and this signifies that the streamwise vortices are characterized by swirling motions with a very small streamwise component. In this case, we have seen that the transverse velocity has a long correlation length in the flow direction and has a streak-like structure, and the streamwise velocity has a short correlation length, which now can be explained by the small streamwise velocity component in the streamwise vortices.

5.2. *Scalar field*

In this section, the evolution of the three passive scalar fields with steady and linear mean scalar gradients in the x_1-, x_2- and x_3-directions is studied by means of the DNS and RDT. The corresponding passive scalar will be denoted by θ_1, θ_2 and θ_3, respectively.

5.2.1. *Scalar fluctuations*

The dimensionless ratio of scalar versus velocity fluctuations is defined as

$$B_\alpha = \frac{\theta'_\alpha/G}{q/S}, \tag{5.6}$$

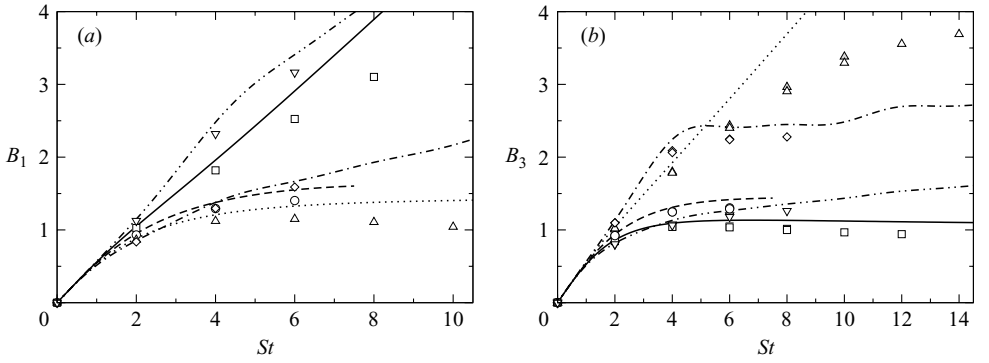

FIGURE 24. Time development of the dimensionless parameter (*a*) B_1 (only series *A*) and (*b*) B_3. Symbols and lines as in figure 3.

where θ'_α is the root mean square of the scalar fluctuations and $q^2 = 2K$. The time development of this relative strength of scalar fluctuations versus velocity fluctuations has been displayed in figure 24 for the five different rotation numbers. Both DNS results and RDT predictions are plotted. Initially, the ratio is zero because there are no scalar fluctuations at $St = 0$, but then it grows because of the presence of the mean scalar gradient. In some cases, the relative intensity seems to reach an asymptotic value at the end of the simulations, but the simulation time was, in general, too short to reach an asymptotic state. This is a difference from the experiments of Tavoularis & Corrsin (1981) and DNS of Rogers *et al.* (1989) where the relative intensity quickly reached an asymptotic value because they used a lower shear rate. Nevertheless, at $R = 0$, θ'_1 is considerably larger than θ'_3, in agreement with the DNS of Rogers *et al.* (1989). The effect of rotation on the relative strength of the scalar fluctuations is significant. In the case with the mean scalar gradient in the x_1-direction, the DNS show that at $R = 0$ and $R = 1/2$, B_1 is larger than when the rotation number is negative (figure 24*a*). At $R = -1$ and $R = -3/2$, B_3 is larger than in the other cases. The RDT predictions agree, in general, quite well with the DNS, but some discrepancies can be seen at larger *St* values.

The change of the structure of the turbulent flow field by rotation influences in its turn the structure of the scalar field. This is observable in figure 25 where visualizations of the instantaneous scalar fluctuations in a plane perpendicular to the flow direction are presented. Small plume-like structures in the scalar field with a streamwise mean gradient can be observed at $R = 0$ (figure 25*a*), but these structures are absent at $R = -3/2$ (figure 25*b*). Plume-like structures are also present in the scalar field with a spanwise mean gradient at $R = -1/2$ (figure 25*c*), but at $R = 1/2$, the structures are more streak-like and elongated in the spanwise direction. Note the very thin scalar structures at $R = 1/2$, which are probably caused by intense strain in the (x_2, x_3)-plane. A possible origin of the plume-like structures is scalar transport by the streamwise vortices which are more dominantly present at $R = 0$ and $R = -1/2$ than at $R = -3/2$ and $R = 1/2$ as we have seen before and are therefore probably responsible for a significant part of the scalar transport. At $R = 0$, the structures in the scalar field with a transverse mean gradient (figure 25*e*) seem to be smaller than at $R = -1$, where again plume-like structures can be observed (figure 25*f*), but this is not surprising because of the presence of many streamwise vortices in this case, as shown before.

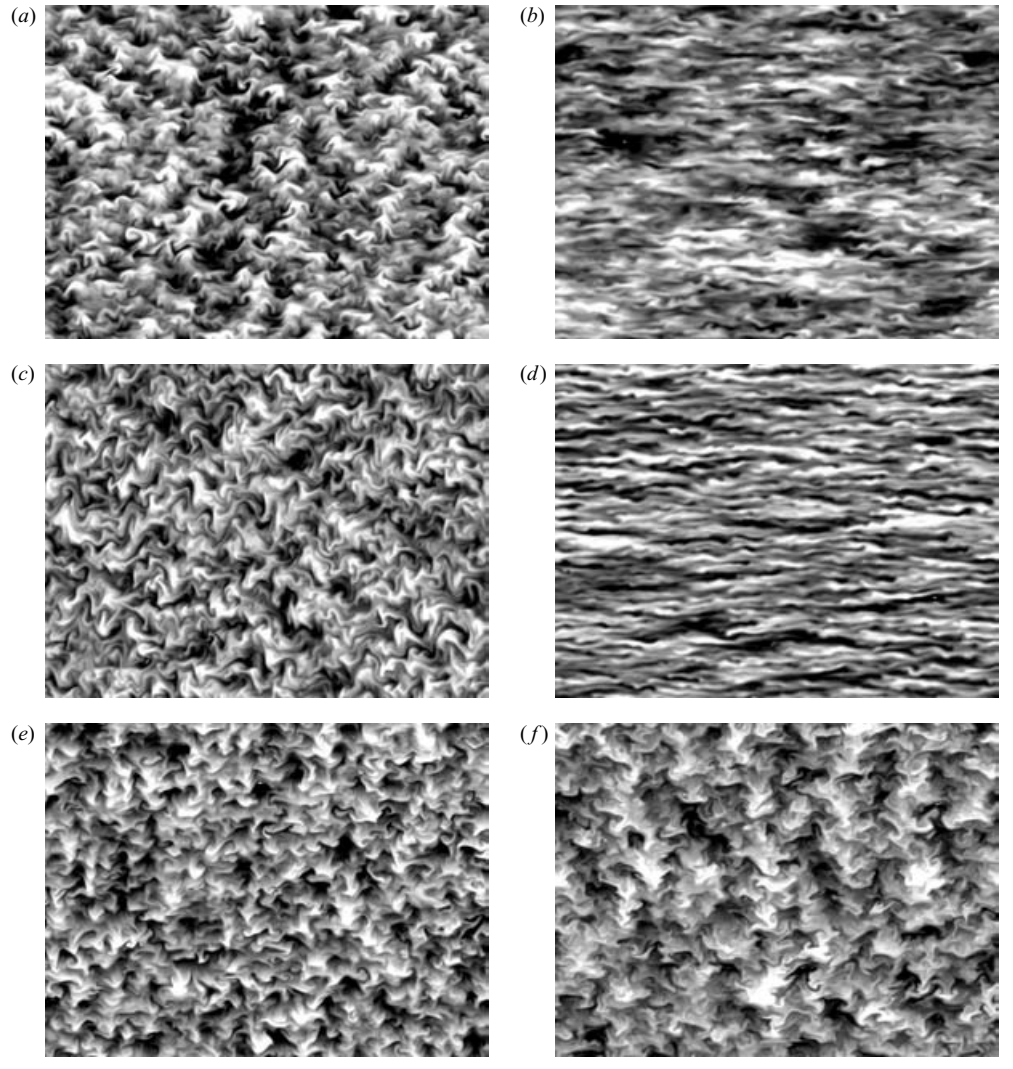

FIGURE 25. The instantaneous scalar fluctuations in an (x_2, x_3)-plane. θ_1 at (*a*) $R = 0$, $St = 8$ and (*b*) $R = -3/2$ and $St = 6$; θ_2 at (*c*) $R = -1/2$, $St = 6$ and (*d*) $R = 1/2$ and $St = 6$; θ_3 at (*e*) $R = 0$, $St = 12$ and (*f*) $R = -1$ and $St = 14$.

5.2.2. *Turbulent scalar fluxes*

The turbulent scalar flux is affected by mean shear and rotation, as can be seen in (2.11), and does not in general, align with the mean scalar gradient (Tavoularis & Corrsin 1981), but our knowledge about the effect of rotation on turbulent scalar transport is limited and therefore a detailed analysis presented.

The scalar–velocity correlation coefficient is defined by (no summation of repeated indices)

$$\zeta_i^\alpha = \overline{u_i \theta_\alpha} / u_i' \theta_\alpha', \tag{5.7}$$

where u_i' and θ_α' are the root mean square of the velocity and scalar fluctuation. Figure 26 presents ζ_1^1 and ζ_3^1 obtained from DNS and RDT predictions. At $R = 0$, ζ_1^1 shows a large negative correlation, but there is also a small scalar flux component

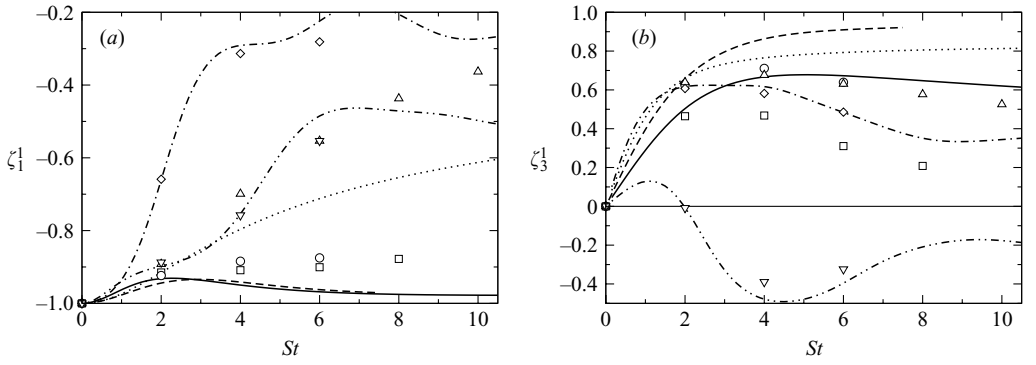

FIGURE 26. Time development of the scalar flux coefficient (*a*) ζ_1^1 and (*b*) ζ_3^1. Symbols (only series *A*) and lines as in figure 3.

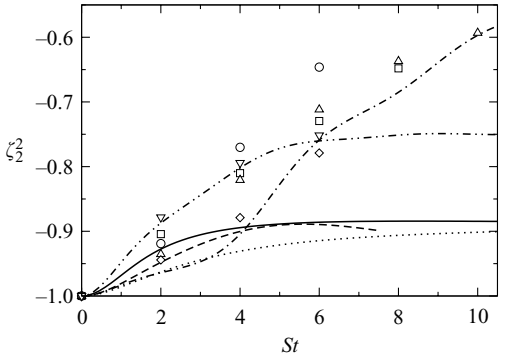

FIGURE 27. Time development of the scalar flux coefficient ζ_2^2. Symbols (only series *A*) and lines as in figure 3.

in the transverse direction shown by figure 26(*b*). The decrease of ζ_3^1 as seen in the DNS is not predicted by RDT. The differences between the RDT predictions and DNS regarding scalar fluxes is caused by differences in velocity fluctuations and the destruction term and the absence of the slow pressure-scalar–gradient correlation in the RDT, see (2.11). The correlation ζ_1^1 has at $R=-1/2$ a large negative correlation as well, but at $R=-1$, ζ_1^1 has a relatively small negative value at the end of the simulation. This is probably a consequence of the cancellation of the second and third production term on the right-hand side of (2.11) at $R=-1$. The RDT predicts a decrease of ζ_1^1, but not as rapid as the DNS. Also at $R=1/2$ and $R=-3/2$, rotation strongly reduces ζ_1^1. In all cases, except at $R=1/2$, ζ_3^1 is positive because the production term due to the mean scalar gradient is positive. At $R=1/2$, this production term of $\overline{u_3\theta}_1$ is small because $\overline{u_1u_3}$ is small, but the third term on the right-hand side of (2.11) is negative, leading to a negative ζ_3^1.

The correlation coefficient ζ_2^2 is also affected by rotation as we see in figure 27, but not as much as the other scalar–velocity correlations. At $R=-3/2$ and $R=1/2$, the RDT predictions and the DNS agree quite well, but at the other rotation numbers, RDT predicts stronger negative correlations than the DNS.

Figure 28 presents ζ_1^3 and ζ_3^3. At $R=0$, $\zeta_3^3=-0.41$ at $St=12$ in the DNS, which is close to $\zeta_3^3=-0.45$ obtained by Tavoularis & Corrsin (1981) and Rogers *et al.* (1986), but in these investigations $\zeta_1^3 \simeq 0.60$, which is considerably smaller than

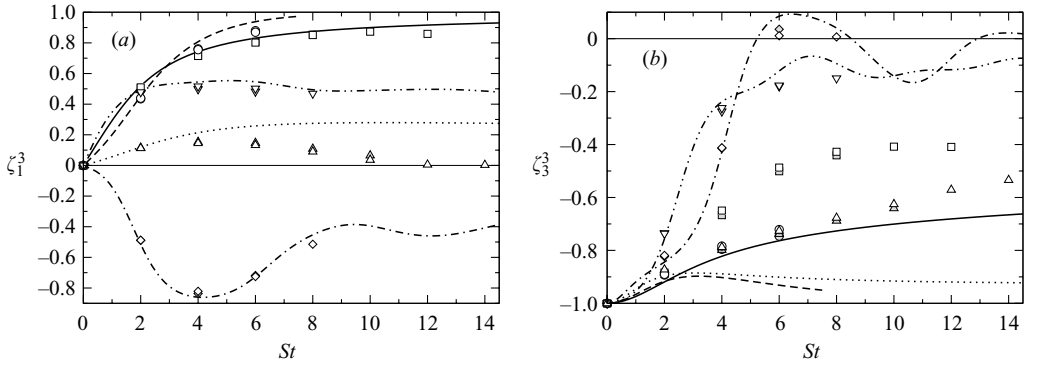

FIGURE 28. Time development of the scalar flux coefficient (*a*) ζ_1^3 and (*b*) ζ_3^3. Symbols and lines as in figure 3.

$\zeta_1^3 \simeq 0.86$ we observed at $St = 12$ in the DNS. A higher shear rate thus gives stronger streamwise scalar–velocity correlations. At $R = -1/2$, the scalar fluctuations are strongly correlated to the transverse and streamwise velocity fluctuations, as shown by the large positive and negative values of ζ_1^3 and ζ_3^3, respectively. At $R = -1$, ζ_3^3 has also large negative values, but $\zeta_1^3 \simeq 0$. This implies that the first product term in the transport equation of $\overline{u_1\theta}_3$ given by (2.11) is balanced by $\Pi_{\theta 1}$ and $\varepsilon_{\theta 1}$ because the second and third terms on the right-hand side cancel each other at $R = -1$. At $R = -3/2$, ζ_3^3 becomes slightly positive at $St = 6$ according to the DNS and RDT predictions, which implies that there is a small counter gradient scalar flux, although it is very small in the DNS. The counter gradient flux is the result of the scalar flux interacting with the rotation which gives a positive contribution in the transport equation, (2.11), for $\overline{u_3\theta}_3$ because $\overline{u_1\theta}_3$ is negative at $R = -3/2$. In this case, ζ_1^3 is negative because the sum of the second and third production terms of $\overline{u_1\theta}_3$ on the right-hand side of (2.11) equals $S\overline{u_3\theta}_3/2$ and is negative until $St = 4$ and the first term is small because $\overline{u_1u_3}$ is small. This is, of course, a simplified explanation because the pressure-scalar–gradient correlation and the destruction terms also play a role.

The RDT predictions in the two stabilized cases, $R = -3/2$ and $R = 1/2$, agree quite well with the DNS, but in the other cases, RDT predicts correlations that are too strong between scalar and transverse velocity fluctuations.

We can gain further insight by studying the direction of the turbulent scalar flux at different rotation numbers. The angle α_θ of the mean turbulent scalar fluxes for the cases with a streamwise or transverse mean scalar gradient is defined as

$$\alpha_\theta = \tan^{-1}(\overline{u_3\theta}/\overline{u_1\theta}), \tag{5.8}$$

and is the inclination angle of the scalar fluxes with the x_1-axis. The scalar flux for the case with a spanwise mean gradient is always aligned with the mean scalar gradient because $\overline{u_1\theta}_2 = \overline{u_3\theta}_2 = 0$ owing to flow symmetry.

Figure 29(*a*) presents the time development of α_θ for the cases with a streamwise mean scalar gradient. Note that in this case, $\alpha_\theta = 0^\circ$ implies a scalar flux down the mean gradient. It is obvious that the rotation has a large influence on the direction of the turbulent scalar flux. At $R = 1/2$ and $R = 0$, the scalar flux has a small positive and negative angle with the streamwise axis, respectively, but in the other cases the scalar flux has a large negative angle with the mean scalar gradient. In the case $R = -1$, $\alpha_\theta = -79^\circ$ at $St = 10$, implying that the scalar flux is almost perpendicular to the mean gradient.

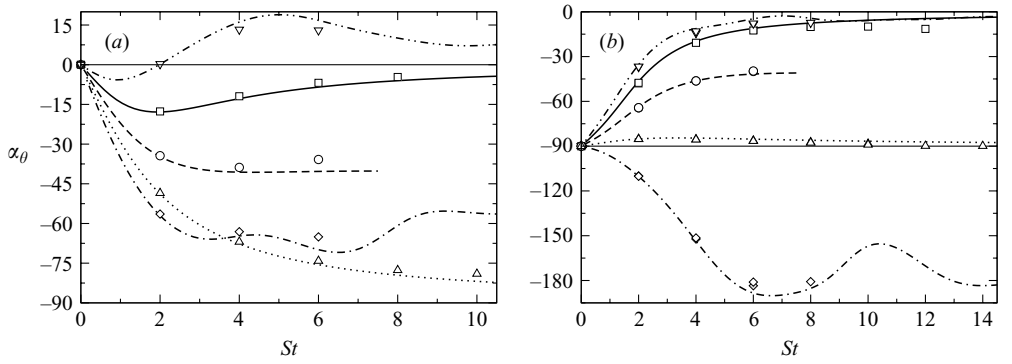

FIGURE 29. Time development of α_θ for the scalar with a (*a*) streamwise (only series *A*) and (*b*) transverse mean scalar gradient. Symbols and lines as in figure 3.

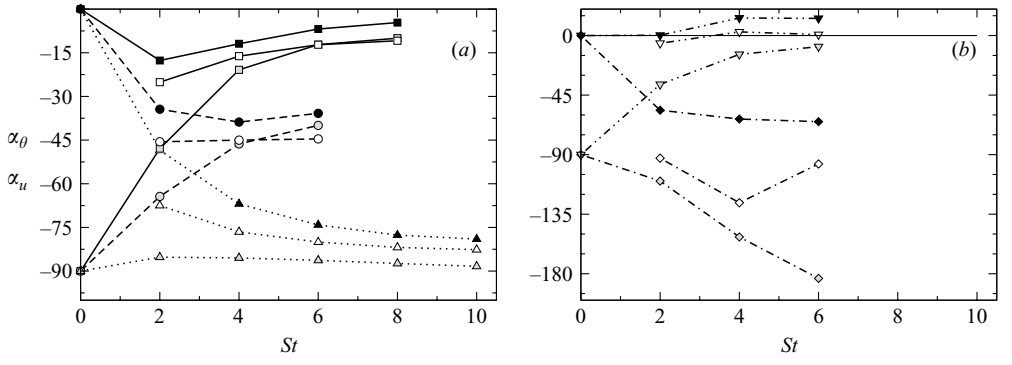

FIGURE 30. Time development of α_u (open symbols) and α_θ for θ_1 (filled symbols) and θ_3 (grey symbols), extracted from the DNS. (*a*) shows the results of the cases (□——□), $R=0$; (○ – –○), $R=-1/2$; (△ · · · △), $R=-1$; and (*b*) shows the results of the cases (▽ – · · –▽), $R=1/2$; (◇ – · – ◇), $R=-3/2$.

Figure 29(*b*) shows the time development of α_θ for the cases with a transverse mean scalar gradient. At $R=-1$, α_θ is close to -90° during the entire simulation, implying a close alignment between the scalar flux and the mean scalar gradient. On the other hand, at $R=-1/2$ and especially at $R=0$ and $R=1/2$, the scalar flux vector has a large component in the streamwise direction at larger St values. The case $R=-3/2$ has also a large scalar flux component in the streamwise direction at larger St values, but the direction of the scalar flux is almost opposite to the direction of the scalar flux at $R=0$. Moreover, the scalar flux has a small counter gradient component in this case as we have observed before. The RDT predictions correspond well in all cases with the DNS and this signifies a large influence of the linear effects on the direction of the scalar transport.

The large variation of the direction of the scalar flux with different rotation numbers is quite remarkable, but some understanding for this large variation can be obtained when the principal angle of the Reynolds stress tensor α_u and the inclination angle of the scalar fluxes α_θ are compared. In figure 30, the time development of those two angles, extracted from the DNS, has been displayed. The close connection between the large-scale structure of the turbulent flow field and the turbulent transport of scalars is apparent. In all cases, except at $R=-3/2$, the turbulent scalar flux rapidly aligns

		Sc_t for θ_1		Sc_t for θ_2		Sc_t for θ_3	
R	St	DNS	RDT	DNS	RDT	DNS	RDT
1/2	6	−0.005	−0.011	−0.005	−0.010	−0.10	−0.31
0	8	0.05	0.03	0.24	0.11	0.97	0.78
−1/2	6	0.42	0.38	0.82	0.63	0.54	0.47
−1	10	0.86	0.44	0.08	0.03	0.04	0.02
−3/2	6	−0.07	−0.12	−0.007	−0.010	0.31	0.17

TABLE 3. The turbulent Schmidt number Sc_t for the scalars with a streamwise, spanwise and transverse mean gradient, respectively. Data are obtained from the DNS, series *A* and RDT.

itself with the principal axes of the Reynolds stress tensor. The same observation, but only for a non-rotating homogeneous shear flow, has been made by Rogers *et al.* (1989). The scalar flux vector is thus, in general, aligned with the direction of the strongest velocity fluctuations. The exception is the case $R=-3/2$ where the scalar flux with the transverse mean gradient is almost perpendicular to the direction of the strongest velocity fluctuations at $St=6$.

The streamwise vortices observed in the cases $R=0$, $-1/2$ and -1 might also play an important role in the transport of the scalars. This is, in fact, indicated by the plume-like structure of the scalar field (figure 25). At $R=0$, the streamwise vortices appear to have a large streamwise velocity component, as shown in figure 23 by means of the PDF of the fluctuating relative helicity density, and can therefore induce a large streamwise scalar transport, which is what we observe. At $R=-1$ on the other hand, the streamwise vortices have a small streamwise velocity component which can cause a preferential scalar transport in the transverse and spanwise direction rather than in the streamwise direction and this is confirmed by the results of the DNS.

The simplest model for the scalar flux is based on a gradient diffusion assumption

$$\overline{u_i\theta} = -\frac{\nu_t}{Sc_t}G_i \tag{5.9}$$

where ν_t is the turbulent viscosity, which is in the present case equal to $-\overline{u_1u_3}/S$, and Sc_t is the turbulent Schmidt or Prandtl number. This model predicts a scalar flux down the mean gradient which is thus inappropriate for the present case. In addition, Sc_t is assumed to be a constant and of order one, but Rogers *et al.* (1989) showed that Sc_t strongly depends on the direction of the mean scalar gradient. Table 3, listing Sc_t computed at the end of the DNS, shows that Sc_t does not depend only on the direction of the mean scalar gradient, but also strongly on the rotation number. At $R=0$, for instance, Sc_t for the scalar with transverse mean gradient is of order one in agreement with the value found in other shear flows, but at $R=-1$, it is much smaller. Even negative turbulent Schmidt numbers are observed at $R=-3/2$ and $R=1/2$ which is not due to counter gradient fluxes, but is a consequence of negative equivalent turbulent viscosities. The positive Schmidt number for θ_3 at $R=-3/2$ is due to the counter gradient flux and the negative turbulent viscosity. RDT predictions of Sc_t are also given in table 3 and they show similar trends regarding the influence of the rotation number to the results obtained from DNS. In a few cases, however, there are significant differences between the predictions of RDT and DNS, for example, at $R=-1$, where the DNS gives a significantly larger value for Sc_t than the RDT in the case of a streamwise mean scalar gradient.

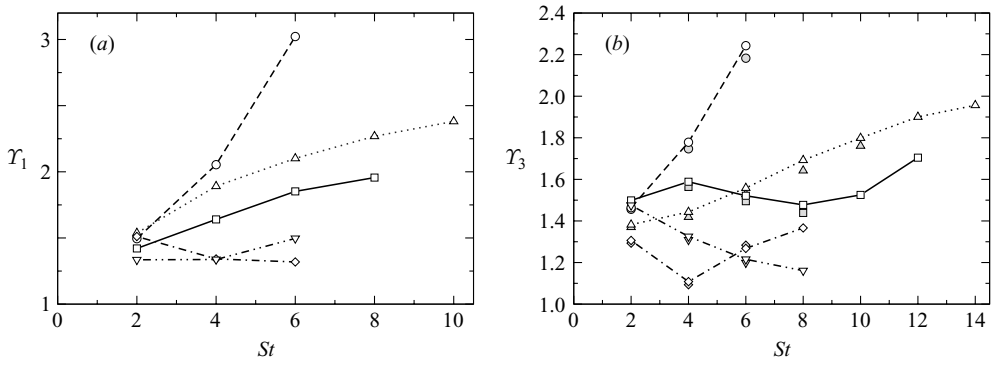

FIGURE 31. Time development of (*a*) Υ_1 (only series *A*), (*b*) Υ_3 (grey symbols: series *A* and open symbols: series *B*). Data are obtained from DNS and symbols and lines are as in figure 30.

5.2.3. *Time-scale ratios*

An often used model for the scalar dissipation is the assumption of a constant ratio of turbulence time scale versus scalar time scale $\Upsilon_\alpha = (2K/\varepsilon)/(\overline{\theta_\alpha\theta_\alpha}/\chi)$ (no summation of repeated indices), where the scalar dissipation $\chi = \kappa\overline{(\partial\theta_\alpha/\partial x_j)(\partial\theta_\alpha/\partial x_j)}$ (only summation of the index j). The time development of this time-scale ratio for the scalars with mean gradients in the streamwise and transverse directions extracted from the DNS, is presented in figure 31. In the DNS of non-rotating homogeneous shear flow of Rogers *et al.* (1989), the time-scale ratio had a value between 1.5 and 2.0, depending on the direction of the mean scalar gradient. In the present case, we observe at $R = 0$ a variation of the time-scale ratio with the mean scalar gradient direction as well, but it does not yet reach an asymptotic value. Of importance is the large variation of the time-scale ratios with the rotation number. At $R = -1/2$, the time-scale ratios reach large values compared to the other cases, especially the scalar with a streamwise mean gradient, as can be seen in figure 31, and the figure indicates that the time-scale ratios may even become larger if the simulations are continued. On the other hand, in the two stabilized cases $R = -3/2$ and $R = 1/2$, the time-scale ratios have small values compared to the other cases.

6. Conclusions

The time development of uniformly sheared homogeneous turbulent flows in a frame rotating around the spanwise axis has been studied by means of a series of direct numerical simulations (DNS). Together with the flow field, the development of a passive scalar field with mean gradients in the streamwise, spanwise and transverse directions, respectively, was investigated in order to clarify the influence of rotation on scalar transport. A relatively high shear rate has been applied in the present study with the aim of approximating the conditions of the near-wall region of turbulent boundary layers. It was therefore anticipated that rapid distortion theory (RDT), based on a linearized set of equations, would give a good description of the observed phenomena.

Several cases have been simulated with varying rotation numbers. In the case $R = 2\Omega/S = -1/2$, the rotation strongly destabilized the flow, resulting in a much more rapid growth of the turbulent velocity fluctuations than in the non-rotating case. In two cases, $R = -3/2$ and $R = 1/2$, the rotation stabilized the flow, leading to

a decay of the turbulent kinetic energy. The anisotropy of the turbulence was also strongly affected by the rotation. Predictions of RDT agreed, in general, quite well with the fully nonlinear DNS, but a closer examination revealed that, even though the applied shear rate was high, nonlinear effects gained in importance during the simulations and sometimes clearly affected the flow. At $R=0$, for instance, the kinetic energy has an exponential growth at larger St values in the DNS, whereas the RDT predicts an approximately linear growth. The importance of the nonlinear processes was apparent in the development of the slow pressure–strain correlations associated with nonlinear processes, which were, in a couple of cases, of the same order or larger than the rapid pressure–strain correlations associated with linear processes. The strongest nonlinear effects were observed at $R=0$, where the transverse velocity fluctuations were much more intense in the DNS than in a simulation without the nonlinear terms.

In the non-rotating case, the streamwise velocity field had a streak-like structure and the vorticity field showed streamwise vortex tubes and some hairpin-like vortex structures, although it changed later in the DNS because then the long streamwise vortices disappeared and the vorticity field became more isotropic. At earlier times, these structures are, indeed, quite similar to those in boundary layers. The structures drastically changed, however, under the influence of rotation. In the case of zero absolute mean vorticity $R=-1$, the transverse velocity field and not the streamwise velocity field had a streak-like structure, and very elongated streamwise vortex tubes were observed. An examination of the helicity showed a predominant swirling motion in the streamwise vortices with a small streamwise velocity component at $R=-1$, whereas at $R=0$, the helical motion in the streamwise vortices had a large streamwise component.

The results presented regarding the influence of rotation on passive scalar transport in a homogeneous shear flow show interesting effects of rotation on turbulent scalar transport. Scalar–velocity correlations were significantly affected and could be strongly reduced or enhanced by rotation. The direction of the turbulent scalar flux also showed large variations, depending on the rotation number. It was shown that the scalar flux vector aligned itself with the direction of the strongest turbulent velocity fluctuations at different rotation numbers. Some of the phenomena, such as the influence of rotation on the scalar flux direction, could be fairly well predicted by RDT, revealing that linear processes are important for scalar transport in rapidly sheared flows, but the scalar–velocity correlations showed large differences in the RDT and DNS in a couple of cases, especially for the transverse scalar–velocity correlation at $R=0$, $-1/2$ and -1, proving the importance of nonlinear processes for scalar transport.

The ratio of turbulent time scale versus scalar time scale, characterizing small-scale mixing, was affected by rotation as well. In the case where rotation destabilized the flow, the ratio of time scales was smaller and at $R=-1/2$ larger than at $R=0$.

The statistics of the Reynolds stresses and pressure–strain correlations presented in this study are useful for the modelling of turbulent shear flows where rotation or streamline curvature plays a role, or for the modelling of rapidly distorted and rotating flows. Scalar transport modelling in rotating turbulent flows has been relatively neglected, although it can be argued that it is of relevance in many practical situations. This study has, therefore, important implications because it has clearly been proved that the effect of rotation on scalar transport is significant and must be taken into account properly. The concept of gradient diffusion fails to describe the variation of the scalar flux direction and the assumption of constant turbulent Schmidt number does not hold with varying rotation numbers. If we try to model scalar transport in

rotating flows, it is thus desirable to consider algebraic scalar flux models, because they are, in principal, able to take into account the influence of rotation. They have been tested only for non-rotating cases so far, but it is of interest to investigate their ability to predict turbulent scalar transport in rotating flows.

The author wishes to thank Anshu Dubey and the Astronomy & Astrophysics Department of the University of Chicago for making their numerical code available, and Arne Johansson, Erik Lindborg, Stefan Wallin and Professor A. Yoshizawa for the valuable discussions and comments. The financial support from the Swedish Research Council and the Göran Gustafsson Foundation is gratefully acknowledged.

Appendix A. Analysis of the stability of rotating homogeneous shear flows using the simplified Reynolds stress equations

It is enlightening to consider the simplified Reynolds stress equations because these explain, at least in a qualitative manner, some of the observed phenomena. A more extensive analysis using the simplified Reynolds stress equations is given by Tritton (1992) (see also Leblanc & Cambon 1997). The simplified Reynolds stress equations read

$$\frac{\partial \overline{u_1 u}_1}{\partial t^*} = -2\overline{u_1 u}_3(1+R), \tag{A 1}$$

$$\frac{\partial \overline{u_2 u}_2}{\partial t^*} = 0, \tag{A 2}$$

$$\frac{\partial \overline{u_3 u}_3}{\partial t^*} = 2\overline{u_1 u}_3 R, \tag{A 3}$$

$$\frac{\partial \overline{u_1 u}_3}{\partial t^*} = \overline{u_1 u}_1 R - \overline{u_3 u}_3(1+R), \tag{A 4}$$

where $t^* = St$. The pressure–strain correlations and the dissipation terms are neglected in this analysis. The equations without the pressure terms show, in a quantitative way, the role of the Coriolis term regarding the stability of the flow because the spectral modes which are mostly affected by the Coriolis force are the spanwise modes (Leblanc & Cambon 1997) for which the pressure effects vanish (Salhi, Cambon & Speziale 1997). However, the influence of the pressure is not negligible as seen in the present DNS and RDT and shown by Salhi & Cambon (1997).

Combining the simplified Reynolds stress equations, we can derive for $\overline{u_1 u}_3$ and the turbulent kinetic energy, respectively,

$$\frac{\partial^2 \overline{u_1 u}_3}{\partial t^{*2}} = -4\overline{u_1 u}_3(1+R)R, \tag{A 5}$$

$$\frac{\partial K}{\partial t^*} = -\overline{u_1 u}_3. \tag{A 6}$$

Considering (A 5), three different cases can be distinguished: $R(R+1) > 0$, $R(R+1) = 0$ and $R(R+1) < 0$.

If $R(R+1) > 0$, i.e. $R > 0$ or $R < -1$, there is a wave-like solution

$$\overline{u_1 u}_3 \sim \exp(2\mathrm{i}\sqrt{R(R+1)}\, t^*). \tag{A 7}$$

The other Reynolds stress components have then also an oscillatory behaviour. The period of the oscillations is $\pi/\sqrt{R(R+1)}$. For $R = 1/2$ and $R = -3/2$, the period is 3.6.

If $R(R+1)=0$, i.e. $R=0$ or $R=-1$, the solution is given by $\overline{u_1u_3}=-c_1t^*-c_2$ where c_1, c_2 are constants. The growth of the kinetic energy is then given by $K=c_1t^{*2}/2+c_2t^*+K(t^*=0)$ and is thus algebraic. If $R=0$, $\overline{u_1u_1}$ has an algebraic growth and $\overline{u_3u_3}$ is constant and if $R=-1$, it is the other way around.

If $R(R+1)<0$, e.g. $-1<R<0$, the solution is

$$\overline{u_1u_3},\, K \sim \exp(2\sqrt{-R(R+1)}\,t^*), \tag{A 8}$$

and the kinetic energy has thus an exponential growth. The fastest growth occurs when $R=-1/2$, then $K \sim \exp(t^*)$.

Appendix B. Some details of the RDT computations

The solution of the set of linear equations, (4.3), is

$$\hat{u}_i(\boldsymbol{k},t)=\exp\left(-\frac{\nu k^2}{S}f(\boldsymbol{k}/k,St)\right)A_{ij}(\boldsymbol{k}/k,t)\hat{u}_j(\boldsymbol{k}',t=0), \tag{B 1}$$

where

$$f(\boldsymbol{k}/k,St)=St\left(1+\frac{k_1k_3}{k^2}St+\frac{k_1^2}{k^2}\frac{(St)^2}{3}\right).$$

The matrix A_{ij} obeys the equation

$$\frac{\mathrm{d}A_{ij}}{\mathrm{d}t^*}=-\mathscr{L}_{iq}A_{qj}, \tag{B 2}$$

where $\mathscr{L}_{ij}$ is defined in (4.3). The initial conditions are $A_{ij}(\boldsymbol{k}',t=0)=\delta_{ij}-k_i'k_j'/k'^2$ where $k_i'=k_i(t=0)$ is the initial wave vector.

The time development of the Reynolds stress tensor is now given by

$$\overline{u_iu_j}=\int A_{ip}A_{jq}\left(\delta_{pq}-\frac{k_p'k_q'}{k'^2}\right)\frac{E(k')}{4\pi k'^2}\exp\left(-2\frac{\nu k^2}{S}f(\boldsymbol{k}/k,St)\right)\mathrm{d}^3\boldsymbol{k}'. \tag{B 3}$$

Using a spherical coordinate system (k',θ,ϕ) for $\boldsymbol{k}'$ and $E(k')$ given by (4.6), (B 3) can be rewritten as

$$\overline{u_iu_j}=\frac{C}{4\pi}\int_0^{2\pi}\int_0^{\pi}A_{ip}A_{jq}\left(\delta_{pq}-\frac{k_p'k_q'}{k'^2}\right)\left[\int_0^{\infty}k'^2\exp\left(-2k'l-2\frac{\nu k^2}{S}f(\boldsymbol{k}/k,St)\right)\mathrm{d}k'\right]\sin\theta\,\mathrm{d}\theta\,\mathrm{d}\phi. \tag{B 4}$$

The integral between brackets can be solved analytically. The solution is

$$-\frac{b^3}{4l^3}\left(-2b+\sqrt{\pi}(2b^2+1)\,\mathrm{e}^{b^2}\,\mathrm{erfc}\,b\right),\qquad b^2=\tfrac{1}{2}S^*\frac{k'^2}{k^2}f(\boldsymbol{k}/k,St),$$

where $\mathrm{erfc}\,b$ is the complementary error function. The expression for the pressure–strain correlation, which is by definition the rapid pressure–strain correlation, reads

$$\Pi_{ij}=\frac{C}{4\pi}\int_0^{2\pi}\int_0^{\pi}\frac{1}{k^2}([(S+\Omega)k_1A_{3q}-\Omega k_3A_{1q}](k_jA_{ip}+k_iA_{jp}))\left(\delta_{pq}-\frac{k_p'k_q'}{k'^2}\right)\left[\int_0^{\infty}k'^2\exp\left(-2k'l-2\frac{\nu k^2}{S}f(\boldsymbol{k}/k,St)\right)\mathrm{d}k'\right]\sin\theta\,\mathrm{d}\theta\,\mathrm{d}\phi, \tag{B 5}$$

with the same analytical solution for the integral between brackets as in (B 4).

If there are no initial scalar fluctuations, the solution of (4.4) for the scalar is

$$\hat{\theta}_i(\boldsymbol{k}, t) = \exp\left(-\frac{\kappa k^2}{S} f(\boldsymbol{k}/k, St)\right) B_j(\boldsymbol{k}/k, t)\hat{u}_j(\boldsymbol{k}', t = 0), \tag{B 6}$$

where θ_i is the scalar with a mean gradient $\boldsymbol{G}$ in the x_i-direction. For θ_i, the vector B_j is the solution of

$$\frac{\mathrm{d}B_j}{\mathrm{d}t^*} = -\frac{G}{S} A_{ij} \exp\left(-(\nu - \kappa)\frac{k^2}{S} f(\boldsymbol{k}/k, St)\right), \tag{B 7}$$

where G is the norm of the mean scalar gradient.

The scalar flux is now derived from

$$\overline{u_j\theta_i} = \int A_{jp} B_q \left(\delta_{pq} - \frac{k'_p k'_q}{k'^2}\right) \frac{E(k')}{4\pi k'^2} \exp\left(-(\nu + \kappa)\frac{k^2}{S} f(\boldsymbol{k}/k, St)\right) \mathrm{d}^3\boldsymbol{k}', \tag{B 8}$$

and the scalar variance from

$$\overline{\theta_i^2} = \int B_p B_q \left(\delta_{pq} - \frac{k'_p k'_q}{k'^2}\right) \frac{E(k')}{4\pi k'^2} \exp\left(-2\frac{\kappa k^2}{S} f(\boldsymbol{k}/k, St)\right) \mathrm{d}^3\boldsymbol{k}'. \tag{B 9}$$

The integrals in (B 8) and (B 9) can then be simplified in the same way as in (B 4) if $Sc = 1$.

For the time integration of (B 2) and (B 7), the spatial integration of (B 4), (B 5), (B 8) and (B 9) and for the computation of erfc b, optimized numerical libraries have been used.

Analytical solutions for (4.3) and (4.4) for homogeneous shear flow without rotation are presented in Rogers (1991). In that paper also short-time and long-time approximations of the Reynolds stresses, scalar fluxes and scalar variances are presented for the case without viscosity and diffusivity.

REFERENCES

Abe, K., Kondoh, T. & Nagano, Y. 1996 A two-equation heat transfer model reflecting second-moments closures for wall and free turbulent flows. *Intl J. Heat Fluid Flow* **17**, 228–237.

Alvelius, K.& Johansson, A.V. 1999 Direct numerical simulations of rotating channel flow at various Reynolds numbers and rotation numbers. In K. Alvelius PhD thesis, Department of Mechanics, KTH, Stockholm, Sweden.

Bardina, J., Ferziger, J. H. & Reynolds, W. C. 1983 Improved turbulence models based on large-eddy simulation of homogeneous incompressible turbulent flow. *Tech. Rep.* TF-19. Stanford University, CA.

Bech, K. H. & Andersson, H. I. 1997 Turbulent plane Couette flow subject to strong system rotation. *J. Fluid Mech.* **347**, 289–314.

Cambon, C., Benoit, J.-P., Shao, L. & Jacquin, L. 1994 Stability analysis and large-eddy simulation of rotating turbulence with organized eddies. *J. Fluid Mech.* **278**, 175–200.

Chong, M. S., Soria, J., Perry, A. E., Chacin, J., Cantwell, B. J. & Na, Y. 1998 Turbulent structures of wall-bounded shear flows found using DNS data. *J. Fluid Mech.* **357**, 225–247.

Ferchichi, M. & Tavoularis, S. 2002 Scalar probability density function and fine structure in uniformly sheared turbulence. *J. Fluid Mech.* **461**, 155–182.

Gatski, T. B. & Wallin, S. 2004 Extending the weak-equilibrium condition for algebraic Reynolds stress models to rotating and curved flows. *J. Fluid Mech.* **518**, 147–155.

Högström, C. M., Wallin, S. & Johansson, A. V. 2001 Passive scalar flux modelling for CFD. In *Proc. of Turbulence and Shear Flow Phenomena II, Stockholm, June 27–29.*

Kida, S. & Tanaka, M. 1994 Dynamics of vortical structures in a homogeneous shear flow. *J. Fluid Mech.* **274**, 43–68.

Kim, J. 1989 On the structure of pressure fluctuations in simulated turbulent channel flow. *J. Fluid Mech.* **205**, 421–451.

Kim, J. & Lim, J. 2000 A linear process in wall-bounded turbulent shear flows. *Phys. Fluids* **12**, 1885–1888.

Komminaho, J. & Skote, M. 2002 Reynolds stress budgets in Couette and boundary layer flows. *Flow Turb. Combust.* **68**, 167–192.

Leblanc, S. & Cambon, C. 1997 On the three-dimensional instabilities of plane flows subjected to Coriolis force. *Phys. Fluids* **9**, 1307–1316.

Lee, M. J., Kim, J. & Moin, P. 1990 Structure of turbulence at high shear rate. *J. Fluid Mech.* **216**, 561–583.

Moser, R. D., Kim, J. & Mansour, N. N. 1999 Direct numerical simulation of turbulent channel flow up to $Re_\tau = 590$. *Phys. Fluids* **11**, 943–945.

Nagano, Y. & Hattori, H. 2003 Direct numerical simulation and modelling of spanwise rotating channel flow with heat transfer. *J. Turb.* **4**, 010.

Poroseva, S. V., Kassinos, S. C., Langer, C. A. & Reynolds, W. C. 2002 Structure-based turbulence model: application to a rotating pipe flow. *Phys. Fluids* **14**, 1523–1532.

Rogers, M. M. 1991 The structure of a passive scalar field with a uniform mean gradient in rapidly sheared homogeneous turbulent flow. *Phys. Fluids* **3**, 144–154.

Rogers, M. M., Mansour, N. N. & Reynolds, W. C. 1989 An algebraic model for the turbulent flux of a passive scalar. *J. Fluid Mech.* **203**, 77–101.

Rogers, M. M. & Moin, P. 1987 The structure of the vorticity field in homogeneous turbulent flows. *J. Fluid Mech.* **176**, 33–66.

Rogers, M. M., Moin, P. & Reynolds, W. C. 1986 The structure and modelling of the hydrodynamic and passive scalar fields in homogeneous turbulent shear flow. *Dept. Mech. Engng Rep.* TF-25. Stanford University, CA.

Salhi, A. 2002 Similarities between rotation and stratification effects on homogeneous shear flow. *Theor. Comput. Fluid Dyn.* **15**, 339–358.

Salhi, A. & Cambon, C. 1997 An analysis of rotating shear flow using linear theory and DNS and LES results. *J. Fluid Mech.* **347**, 171–195.

Salhi, A., Cambon, C. & Speziale, C. G. 1997 linear stability analysis of plane quadratic flows in a rotating frame with applications to modeling. *Phys. Fluids* **9**, 2300–2309.

Speziale, C. G., Younis, B. A. & Berger, S. A. 2000 Analysis and modeling of turbulent flow in an axially rotating pipe. *J. Fluid Mech.* **407**, 1–26.

Tanaka, M., Yanase, S., Kida, S. & Kawahara, G. 1998 Vortical structures in rotating uniformly sheared turbulence. *Flow Turb. Combust.* **60**, 301–332.

Tavoularis, S. & Corrsin, S. 1981 Experiments in nearly homogeneous turbulent shear flow with a uniform mean temperature gradient. Part 1. *J. Fluid Mech.* **104**, 311–347.

Tavoularis, S. & Karnik, U. 1989 Further experiments on the evolution of turbulent stresses and scales in uniformly sheared turbulence. *J. Fluid Mech.* **204**, 457–478.

Tritton, D. J. 1992 Stabilization and destabilization of turbulent shear flow in a rotating fluid. *J. Fluid Mech.* **241**, 503–523.

Wallin, S. & Johansson, A. V. 2002 Modelling streamline curvature effects in explicit algebraic Reynolds stress models. *Intl J. Heat Fluid Flow* **23**, 721–730.

Wikström, P. M., Wallin, S. & Johansson, A. V. 2000 Derivation and investigation of a new explicit algebraic model for the passive scalar flux. *Phys. Fluids* **12**, 688–702.

Wu, H. & Kasagi, N. 2004 Turbulent heat transfer in a channel flow with arbitrary directional system rotation. *Intl J. Heat Mass Transfer* **47**, 4579–4591.

Zhou, J., Adrian, R. J., Balachandar, S. & Kendall, T. M. 1999 Mechanisms for generating coherent packets of hairpin vortices in channel flow. *J. Fluid Mech.* **387**, 353–396.